Master’s Thesis of Engineering

Stability of Concrete Cylindrical Structures in 3D Printing Process

콘크리트 원형 중공 단면 구조물의
3D 프린팅 출력 중 구조적 안정성

February 2023

Graduate School of Enginerring
Seoul National University
Architecture and Architectural Engineering

Seung Su Jeong

Stability of Concrete Cylindrical Structures in 3D Printing Process

Advisor : Sung Gul Hong

Submitting a master's thesis of
Architecture and Architectural Engineering

December 2022

Graduate School of Engineering
Seoul National University
Architecture and Architectural Engineering

Seung Su Jeong

Confirming the master's thesis written by
Seung Su Jeong

February 2023

Chair	**CHEOL-HO LEE**	**(Seal)**
Vice Chair	**SUNG-GUL HONG**	**(Seal)**
Examiner	**HONG-GUN PARK**	**(Seal)**

Abstract

Stability of Cylindrical Concrete Structures in 3D Printing Process

Jeong, Seung Su
Department of Architecture and Architectural Engineering
College of Engineering
Seoul National University

Preventing the failure by self-weight loading during 3D printing process is a major consideration for the 3D printed structure. Since the fresh state concrete material which has lower stiffness and strength is used during printing, the maximum length that can be printed in a single printing process should be estimated in the design or construction process. The mechanical model is suggested in this paper which can be used for analyzing the mechanical performance and optimizing the priting parameters of the cylindrical structures in 3D printing process. Three types of failure mechanism are considered, such as elastic global buckling, elstic local buckling and plastic collapse, by the column model, shell model and yield criterion, repectively. The model includes the various parameters which are relating to the material properties, geometrical features and printing variables. The curing effect, characteristic of concrete material, has been considred by heterogenous stiffness and strength along the length when modeling the structure. The non-dimensional critical buckling length is first analyized and compared between two buckling model on the design graphs, while the non-dimensional plastic collapse length is predicted on another coordinates. The specific case study that all the paramters are determined shows the process interpreting the numerical analysis results, and governing failure mechanism, lenghth and corresponding buckilng mode are obtained. The linearly assumed curing function is verified from the experiment measuring material properties. Data from the printing test which was conducted with the different sizes of cylindrical structures is compared with the predicted failure length from the model for the validation. The model can be utilized as a tool for exploring the influence of each printing parameter on the mechanical performance of the arbitrary cylindrical structures and predicting the failure length and governing failure mechanism.

Keywords : 3D printing, Cylindrical structure, Heterogeneous material, Buckling, Plastic collapse, Numerical analysis, Design graph

Student Number : 2021-24853

Contents

List of Tables

List of Figures

List of Symbols

d	=	depth of a layer
g	=	gravity acceleration
g_*	=	curing function of material
$\bar{g}_*$	=	curing function in terms of dimensionless Eulerian coordinate
h	=	breadth of a layer (radial thickness of a layer)
h_*	=	curing function for yield strength
$\bar{h}_*$	=	curing function for yield strength in terms of dimensionless Eulerian coordinate
l	=	longitudinal height of structure
l_{cr}	=	critical buckling length
$\bar{l}_{cr}$	=	non-dimensional critical buckling length
l_P	=	plastic collapse length
$\bar{l}_P$	=	non-dimensional plastic collapse length
$\dot{l}$	=	structure growth velocity
$\bar{k}_w$	=	dimensionless wavenumber
n	=	circumferential wavenumber (buckling mode)
n_t	=	number of printed layers defining wavelength of imperfection profile
q	=	body force applied to unit length
s	=	location in which moment equilibrium equation for column model is derived
t	=	concrete age (curing time)

t_{rest} = resting time of material

t_l = height of a printed layer

u = longitudinal displacement

$\bar{u}$ = dimensionless longitudinal displacement

v = circumferential displacement

$\bar{v}$ = dimensionless circumferential displacement

v_n = printing speed of nozzle

w = radial displacement

w^0 = geometric imperfection profile

w^F = deflection under applied load

$\bar{w}$ = dimensionless radial displacement

$\bar{w}^0$ = dimensionless geometric imperfection

$\bar{w}^F$ = dimensionless deflection under applied load

w_m^0 = amplitude of imperfection

$\bar{w}_m^0$ = dimensionless amplitude of imperfection

x = longitudinal coordinate (Largrangian coordinate)

y = circumferential coordinate (Largrangian coordinate)

z = radial coordinate (Largrangian coordinate)

A = cross-sectional area of cylindrical structure

A_{thix} = rate of increase of static yield stress of material

D = average diameter of cross-section

D_0	=	initial flexural rigidiy of material
D_*	=	heterogeneous flexural rigidity
$\bar{D}_*$	=	flexural rigidity in terms of dimensionless Eulerian coordinate
E_0	=	initial stiffness of material
E_*	=	heterogeneous stiffness modulus
$\bar{E}_*$	=	stiffness modulus in terms of dimensionless Eulerian coordinate
I	=	second moement of area of column cross-section
K	=	conversion factor
M	=	external moment
M_{int}	=	internal moment
Q	=	volume of the material discharged per unit time
R	=	radius of cylindrical structure
$\bar{R}$	=	non-dimensional radius
T_l	=	printing period of a layer
U	=	total strain energy
U_b	=	bending strain energy
U_s	=	membrane strain energy due to stretching of mid-surface
V	=	potential energy
X	=	Eulerian coordinate
$\bar{X}$	=	dimensionless Eulerian coordinate
α	=	ratio of layer thickness to radius of structure

δ	=	location of boundary for plastic failure in terms of dimensionless Eulerian coordinate
η_{xx}	=	in-plane force
θ	=	circumferential coordinate
κ	=	location of boundary in terms of dimensionless Eulerian coordinate
μ_p	=	plastic viscosity
ν	=	Poisson's ratio
ξ_E	=	curing rate of stiffness modulus
$\bar{\xi}_E$	=	non-dimensional curing rate of stiffness modulus
ξ_σ	=	curing rate of yield strength
$\bar{\xi}_\sigma$	=	non-dimensional curing rate of yield strength
ρ	=	density of material (concrete)
σ	=	normal stress
σ_c	=	uniaxial compressive strength
σ_p	=	yield strength
$\sigma_{p,0}$	=	initial yield strength
σ_x	=	stress on a bottoom layer
τ_{00}	=	Initial static yield stress of material
τ_{xz}	=	shear stress generated at the interface between adjacent layers
$\bar{\tau}$	=	dimensionless boundary factor
ω	=	factor quantifying influence length of exponential term at the boundary
Π	=	total potential energy

Chapter 1. Introduction

1.1 Background

As the global population continuously increases and the global contruction market is expected to be larger than the present, construction industry is interested in developing construction technologies for the future, considering sustainability, eco-friendliness, and energy saving. In addition, as construction materials, structures and construction methods develop, architectural styles gradually changing from formal to un-formal. Traditional construction methods using concrete material have limitations in following the architectural trends. Thus, 3D printing technology is attracting attention which is already widely used in various fields due to many advantages. The architectural and civil engineering are making great efforts to incorporate the 3D printing technology into the construction field.

Unlike subtractive manufacturing method, SM, 3D printing technology refers to additive manufacturing, AM, technology that produces 3-dimensional object according to computer design by adding materials one layer at a time [1]. Various additive manufacturing techniques have been developed according to the materials and additive methods, and can be divided into seven processes. Material extrusion, binder jetting, directed energy deposition, material jetting, powder bed fusion, sheet lamination abd vat photopolymerization [2]. The 3D printing process used in the construction field so far is FDM, fused depositioin modeling, method among the material extrusion manufacturing process. Since this method has a great advantage of being able to directly extrude concrete materilas, it can replace the traditional construction method in a relatively short period of time. Furthermore, it is suitable for application to the construction filed in that it is the method with the least space constraints during construction and it can be easily introduced.

Table 1-1 Types of additive manufacturing process (Lee et al., 2020)

Process Category	Definition	Related Technology
Material Extrusion, ME	material is selectively dispensed through a Nozzle or Orifice	FDM (Fused Deposition Modeling), DDM (Direct Digital Manufacturing)
Binder Jetting, BJ	a liquid bonding agent is selectively deposited to join powder materials	3DP, IPP, VoxelJet
Directed Energy Deposition, DED	focused thermal energy is used to fuse materials by melting as they are being deposited	LENS, LD, LC, WLAM, WAAM, EBF, PEBF
Material Jetting, MJ	droplets of feedstock material are selectively deposited	Polyjet, MJP, NPJ, DOD
Powder Bed Fusion, PBF	thermal energy selectively fuses regions of a powder bed	SLS, DMLS, SLM, EBM, PEBM
Sheet Lamination, SHL	sheets of material are bonded to form a part	LOM, CAM-LEM, VLM-ST
Vat Photopolymerization, VPP	liquid photopolymer in a vat is selectively cured by light-activated polymerization	SLA, 3PS, DLP

When FEM 3D printing technology is applied to the construction industry, it is possible to digitize all processes from design to construction, reducing labor dependence, which is the cause of low productivity and efficiency, and improving complex interests among the person concerned. In terms of construction, unlike the general reinforced concrete construction method, it does not require a mold, so it can simplify the consruction process of the structure element and increase the degree of freedom of shape, which has great advantages in the construction of atypical architecture. In addition, it is possible to make a fast prototype, and it is relatively advantageous in terms of material or energy consumption and cost. These advantages are why construction industry pay attention to 3D printing technology as a future construction technology.

However, in reality, while some industries and manufacturing fields, such as aerospace, automotive, and medicine, have already applied 3D printing technology to create high productivity, accuracy and efficiency, architecture and civil engineering have relatively slow technological progress and few field applications. The main reason is that the scale of object, which will be printed by 3DP, is large due to the characteristics of the construction field, and structural stability, safety, and reliability should be ensured, so it is still dangerous and inefficient to apply 3DP technology instead of the existing method. In addition, there are limitations in controlling the production environment or various variables that affect the quality of the printed structure, and furthermore, there are many restrictions on field application.

Although applying 3DP technology is difficult due to these characteristics of the construction field, research and development of 3DP related to the architecture and civil engineering have been actively conducted since 2010. The number of papers published since 2010 is approximately twice of the total number of previous papaers, and is rapidly increasing recently [3]. Half of the total studies were conducted in United States and United Kingdom, with about

2 in Korea. Most of the papers written focus on developing materials suitable for 3DP by measuring and evalutating the concrete material properties. This is because due to the characteristics of 3DP, the required performance varies depending on the moving stage of the material, and the material properties vary over time due to the curing effect of the concrete. Figure 1-1 shows the features related to the performance of concrete materials required at each stage from the production of the material to the operation after printing. First, since 3D printer discharges and stacks materials limitedly by a certain volume per unit time, resistance to material separation is required in the production and transportation process so that the discharged materials can be homogeneous. In addition, sufficient fluidity and viscosity are required to pass through the pipe consistenetly carrying the material from the pump to the nozzle. The performances required in the process of discharging and adding the material from the nozzle are extrudability and buildability. The performance of continuous priting of fresh state concrete without breaking is called extrudability, and the performance of adding discharged concrete at a constant height without deformation and collapse is called buildability. This is the most important performance considered in the development of materials for 3D printing, and is related to the rheological properties, viscosity and yield stress. These characteristics are also related to the bond strength between layers that affect the strength of the entire structure in the printing process. In addition, sufficient intial compressive strength of fresh concrete is required to prevent the yield of the bottom layer to the increasing vertical stress as the material is adding. Finally, structures whose printed object has been completed and cured require hardened mechanical performance of the material, such as compressive

strength and bending strength, to satisfy the structural design [4].

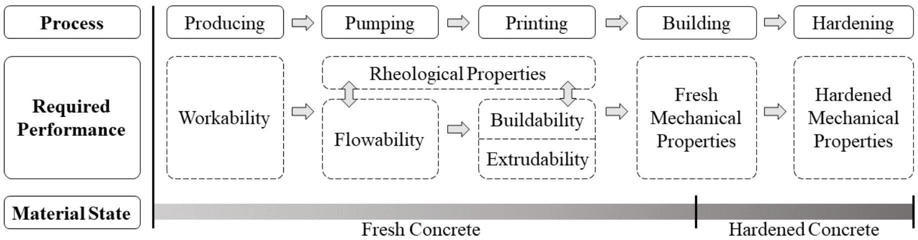

Figure 1-1 Required performance of 3DPC according to the process

There are cases where building have been constructed by applying 3D printing technology from where research has been actively conducted, but research and technology development are relatively slow in Korea and there are few cases of construction. Howere, it has not progressed to the large-scale building construction and commercialization anywhere. This is because previous studies evaluated the performance of the printed structure in material units as mentioned above. In other words, it focused only on the properties of the concrete material, and there are few researches on measuring and evaluating the mechanical performance of the entire structure printed with 3DP technology. Although the performance of the material is satisfying to the design, it is not linked to the performance of entire structure.

Figure 1-2 3D printed bridge and building (from IAAC)

In order to apply FDM concrete 3D printing technology to the construction industry, it is necessary to identify and verify structural performance, stability, by considering the mechanical performance of the entire structure and the influence of various parameters. In particular, the structure in printing process is built by fresh state concrete, which has fluidity, viscosity and low strength and stiffness. Thus, resisting to the failure during construction is more important than after printing completed. For example, since concrete is placed without mold, maintaining its shape without collapse with sufficient material properties and mechanical performance of printing structure is necessary. If the performance is not sufficient, failure may occur due to the occurrence of geometric imperfections, buckling or plastic collapse in 3D printing process. However, quantitatively estimating the performance of the structure during construction is not easy, since diverse printing variables such as printing speed and layer dimensions, material properties such as curing effect, and geometric characteristics of structure affect the mechanical performance in combination. Therefore, in the field, some parameters are generally determined through trial and error methods. Hoeverever, since the size of the printing object is relatively large, determining the variables in this way will result in additional unnecessary costs and inefficiencies. Therefore, in order to improve, it is necessary to develeop a model that can identify parameters that affect the mechanical performance of the entire structure in 3D printing process and predict it.

1.2 Prior research

Suiker developed a model that can determine the mechanical performance of concrete wall structures constructed by 3D printing (3DP) [5]. This model is suitable for the analysis of rectangular wall lay-out types of wall structures with supporting walls as well as walls with boundary conditions such as free, simply-supported or fully clamped. First a simplified 3DP concrete wall with a constant cross-section of the layer and no horizontal curvature is modeled as a plate element. Plate elements have heterogeneous material properties in the length direction due to the curing effect of concrete mateirals, and the non-uniform load generated by the self-weight is set as the main load. The model deals with two types of failure mechanism, elastic buckling and plastic collapse of wall structure. The elastic buckling model formulates the total potential energy and minimizes it to satisfy the equilibrium condition. Governing buckling equation is derived including the boundary condition and the time effect, and non-dimensionless buckling length is calculated by converting original coordinate system to dimensionless. The dimensionless parameters include printing variables, material properties and geometric characteristics, and there three non-dimensional parameters. On the other hand, before buckling occurs, plastic collapse occurs when the self-weight per unit area raches the yield strength of the lowest layer. This failure mode is analysed by two independent parameters and is influenced by the functional form of the curing effect of the material. In the case of a linear function, the non-dimensional plastic collapse length can be expressed explicitly with the dimensionless curing rate. Otherwise, in the form of an exponential function, a nonlinear equation is obtained, and thus a solution may be calculated by a numerical analysis. In conclusion, the simplelysupported wall provides a buckling length as lower bound, the fully-clamped wall provides an upper bound, and the plastic collapse length narrows this range. Therefore, the elastic buckling and plastic collapse model enable accurate prediction of the failure length and failure mechanism for arbitrary wall configuration and printing condition. For the verification experiment, some parameters are fixed to the speicif value, and the buckling length is estimated from the numerical analysis, and the error is within 10% when compared with the experimental result. Suiker's research provides insight into the development of the mechanistic model that can predict the mechanical performance of 3D printing concrete structures and optimize parameters by considering the dead weight and the curing effect of material.

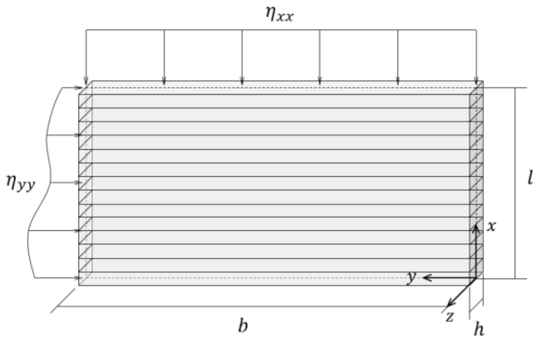

Figure 1-3 Rectangular plate subjected to non-uniform in-plane forces in the mid-plane (modified from Suiker, 2018)

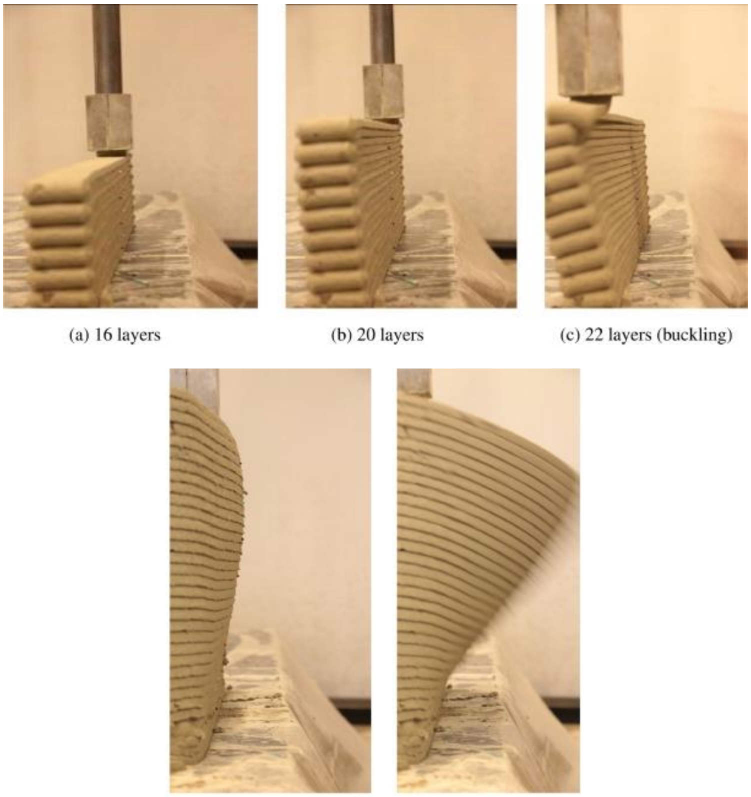

(a) 16 layers (b) 20 layers (c) 22 layers (buckling)

(a) Wall b at the onset of buckling. (b) Wall b during buckling.

Figure 1-4 Buckling of free wall and wall with support wall (Suiker, 2018)

1.3 Objectives

Among the types of walls covered by Suiker's model, simply-supported and fully-clamped walls can not be fully implemented in 3D printing in reality if they are single wall lay-out. Since the concrete is not hardened during construction, the material at the point cannot resist the reaction force and deformation occurs or element breaks. Therefore, the walls which can be constructed with 3DP are a free wall or a rectangular wall lay-out type with supporting wall. The free wall which deos not have a lateral support has very low stiffness, thus buckling occurse easily in printing process. On the other hand, in the case of the rectangular wall lay-out type, the stiffness and performance are increased when the area tangent to the floor is assumed as same as the free wall type. However, as the overall shape is maintained and the circumferential length of the wall increases, the performance of the two types decreases and the difference between the two decrease. Since most of the actual case constructed with 3DP is wall type structures with a long horizontal length, support elements are placed inside the rectangular wall lay-out to compensate for the reduced stiffeness as the horizontal length increases. Wall structure with internal supports have excellent performance during construction, but it is a relatively inefficient method in terms of cost and material consumption.

Figure 1-5 Rectangular wall lay-out with internal support (from Apis Cor)

3D printing concrete structures are designed to have no curvature or constant curvature for ease of construction. Suiker's model is limited to 3DP concrete structures with no curvature, and is suitable for column analysis with rectangular hollow sections as well as wall anyslis. However, predicting the performance for cylindrical structures which have constante curvature, column or wall, with hollow section is not possible. If the area and size of the bottom layer are constant and only the shape of the cross-section changes from square to circular, the cross-section rigidity and stiffness increases with the performance increasing. Therefore, by changing the cross-sectional shape, the sufficient performance can be secured without unnecessary internal support elements and reduce material consumption. If the hollow square structure is designed to be equal to the stiffness of the circular structure, the amount of material used increases. In summary, in order to satisfy a certain structure's performance during 3DP construction, it is efficient and effective to design the layout of the structure in the circular shape rather than rectangular.

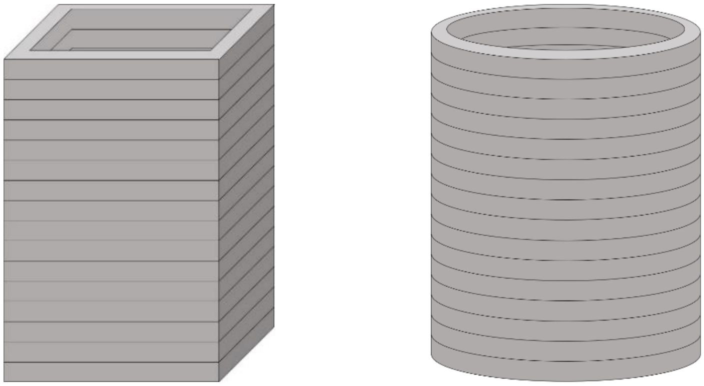

Figure 1-6 Rectangular wall lay-out structure and circular cylindrical structure

However, when printing the circular cylindrical structure, the length and period of a single layer are relatively short, thus a model that accurately predicts the performance of the structure in printing process is needed. Since the ratio of layer height to diameter is small, applying the plate element in Suiker's paper is not appropriate to model cylindrical structures. In addition, new boundary conditions are needed to suit a new model.

When constructing the structure with 3D printing, there are four main failure mechanism during construction, buckling, plastic collapse by material yielding, collapse by geometric imperfections and failure due to displacement accumulation. In general, thin hollow circular structures show various buckling behaviors depending on the diameter - length ratio and thickness - diameter ratio, and can be divided into four types, elastic global buckling, inelastic global buckling, elastic local buckling and inelastic local buckling. When the ratio of thickness to diameter is large, the cross-sectional rigidity is large, and thus the global buckling is expected to be occurred in which the cross-sectional shape is not greatly distorted, and as the ratio becomes smaller, the local buckling behavior is expected.

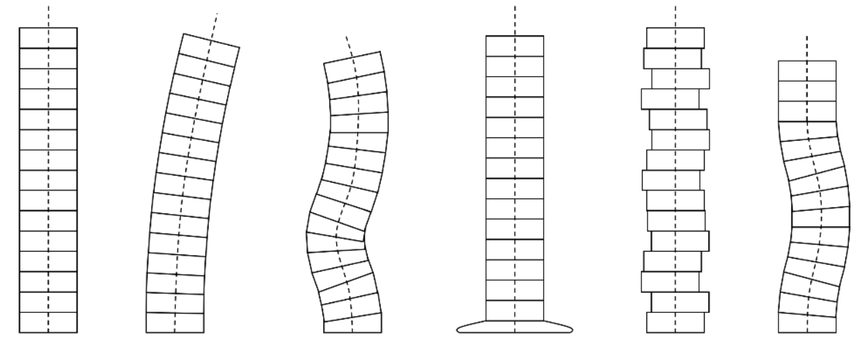

Figure 1-7 Failure behaviors of 3D printed circular structures : (a) geometrically perfect strucure, (b) global buckling, (c) local buckling, (d) plastic collpase, (e) geometric imperfection, (f) failure due to deformation

In this paper, the maximum length and time that can be continuously printed by developing the model that predicts the critical buckling length and plastic collapse length for arbitrary cylindrical structure caused by the self-weight in 3D printing process. The model, considering the stiffness and strength that increases as the length of the strucutre increases, predicts the mechanical performance of the cylindrical structures with various shape ratios and presents a 3D printing design method based on design graphs and validation experiments.

Chapter 2. Models for Numerical Analysis of Cylindircal Structures

2.1 Research Models

The configuration of the 3D printed cylindrical structure carrying out the numerical analysis is shown in the following figure. The height of a layer is h, and the distance from the center of the hollow circular structure to the average height of the layer is R, since the analysis will be proceeded at the mid-plane. The depth of a layer is denoted by d and the overall length of the structure is represented by l. The length l may be the critical buckling length, l_{cr}, or plastic collapse length, l_p, depending on the failure mode of the structure. The smaller of the two length values becomes the governing failure length, l_f. In order to predict this length, a separate analysis model is required for each failure mode. Since the buckling behavior of cylindrical structure varies depending on the geometric ratio, appropriate analysis models are needed.

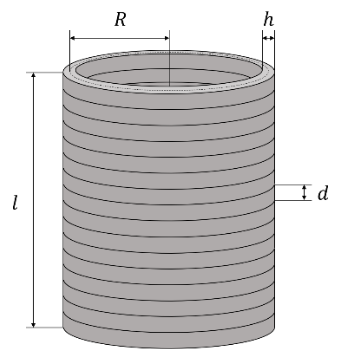

Figure 2-1 Geometric configuration and notation of cylindrical structure

2.1.1 Column model for elastic global buckling

In the case of the cylindrical structure with a large layer thickness – diamter ratio, it is expected that deformation of cross-sectional shape is not significant and then elastic global buckling will occur due to its high flexural rigidity. These structures can be modeled as a column model using beam theory. Assuming the deformation form as soon as buckling begins, the bifurcation approach is used to derive the governing equation with equilibrium conditions [6].

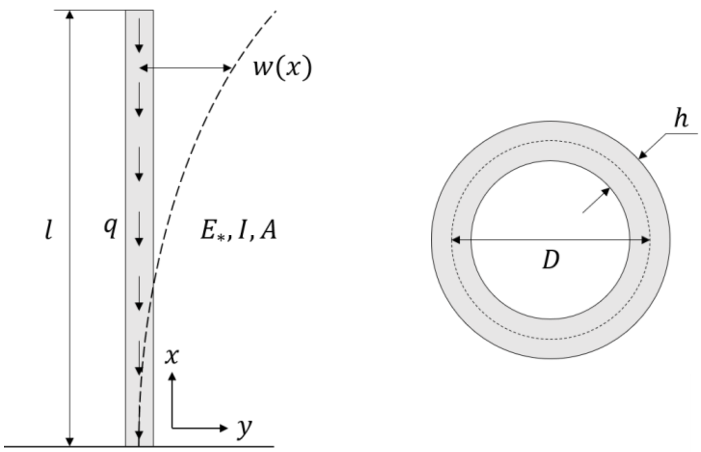

Figure 2-2 Column model for global buckling analysis

2.1.2 Shell model for elastic local buckling

On the other hand, as the ratio decreases, cross-sectional deformation is more likely to occur and large, thus it is appropriate to model the cylindrical structure as a shell element instead of the column. Since the shell elements cannot directly be used to derive the equilibrium equation, this equation is drived by using energy method with minimizing the total potential energy. Unlike the column model that use 2-dimensional coordinate axes (x, y), the shell model performs 3-dimensional analysis, thus it uses a coordinate system representing the length direction x, radius r and rotation angle from the center θ [7].

Although the buckling model is divided into two models according to the expected buckling behavior based on the geometric features of the cylindrical structure, the selection criteria for the models are not clear. Therefore, this paper applies both models to arbitrary cylindrical structures with various geometric characteristics to proceed numerical analysis and compare the results between two models to specify the model selection criteria.

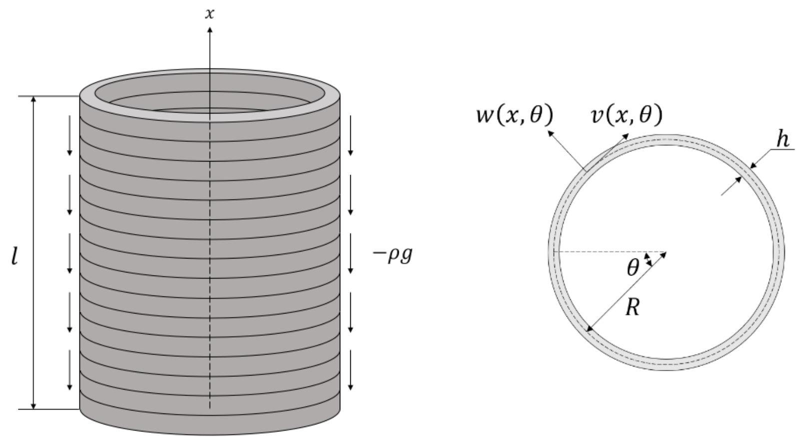

Figure 2-3 Shell model for local buckling analysis

2.1.3 Yield criterion for plastic collapse at the bottom of structure

In addition to the failure cased by the buckling during construction, the 3D printed structure also has a case of the plastic collapse due to the material yielding by the dead weight. As the length of the structure increases, the weight per unit area applied to the bottom layer reaches the compressive strength of the material. By placing the stress when the bottom layer yields and the yield strength of the material, the plastic model can be expressed by an equation. This model is highly influenced by the initial compressive strength of the fresh concrete, the growth rate of strength and the form of the curing function, and the formulation of the model varies depending on the characteristics of the material [5].

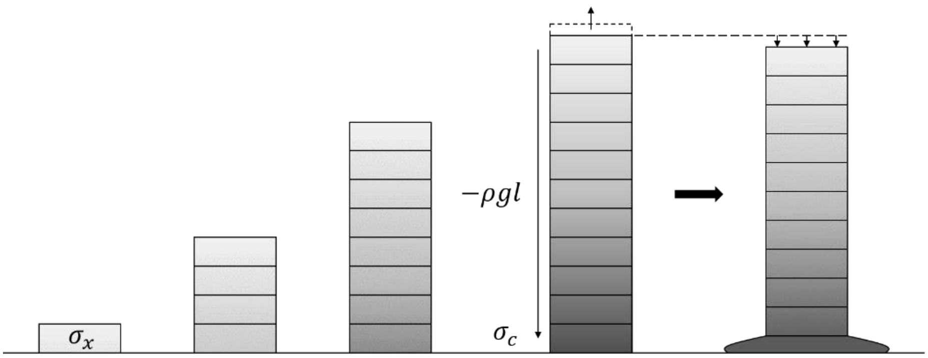

Figure 2-4 Plastic collapse mechanism

2.2 Assumption and Coordinate System

2.2.1 Growth of structure length subjected to self-weight load

The main load causing the failure of the structure in 3D printing process is the structures's own weight. Therefore, in the three models mentioned at previous chaper, the mechanical performance is measured by considering only the dead weight of the structure. It is assumed that the load at a specific location increasese linearly as the length increases. This assumption means that the length of the structure increases to a constant speed, $\dot{l}$, and a symmetrical load, constant loading on a layer, is applied relative to the central axis of the cylindrical structure.

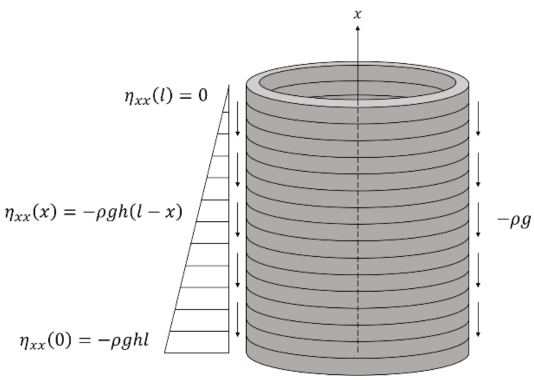

Figure 2-5 Linearly increasing self-weight subjecting to cylindrical structure

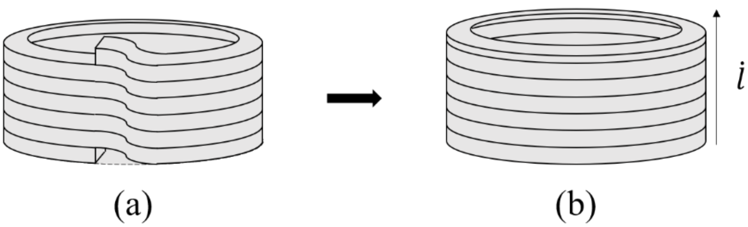

Figure 2-6 Length growth for (a) real printing process and (b) assumption

2.2.2 Curing function of stiffness modulus and compressive strength

The properties of printing material that affects the mechanical performance of the 3D printed structure during construction, initial elastic modulus and initaial compressive strength of the fresh concrete, can be assumed in the form of linear of exponential functions over time. In particular, the exponentially-decaying curing function appears when the curing process is accelerated by external stimulus, such as UV light or heat. Typical concrete amterials are assumed in linear functional form. Therefore, assuming the stiffness and strength as a linear increasing in this model, the model includes the heterogeneous property of the material in the length direction in printing process. This assumption will be verified through experiments.

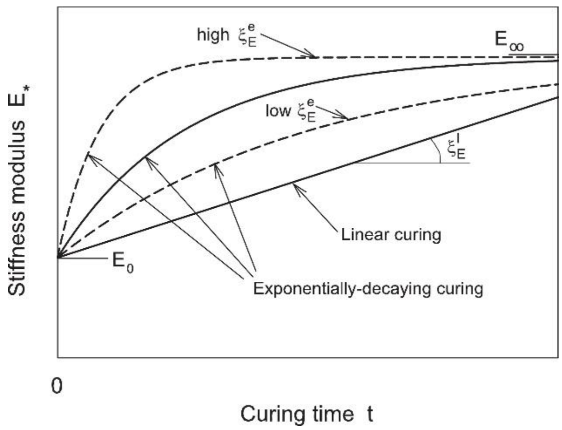

Figure 2-7 Linear and exponentially-decaying curing funcions (from Suiker)

2.2.3 Coordinate systems

The curing effect of concrete material is a function of time. The time when the bottom layer material is cured, in other words, the time it takes to build up to a certain length after the bottom layer is printed, is expressed in t, and the length, l, is expressed by multiplying time t and growth speed of length $\dot{l}$. Since time t is based on the bottom layer, the time taken from a specific location to the currelty printed length can be calculated using both location x and time t variables to determine the degree of curing of the material at the specific location. However, in this model, since the length l is a variable to be found, time t is also treated as a variable. Ultimately, there are two variables in the curing function, location x and time t, thus a new coordinate system is needed to consider the two together. Therefore, if the coordinate system is set in terms of the current position of the nozzle, the reference point for measuring the location of the specific material and the time taken becomes the same. This coordinate system is called the Eulerian coordinate system.

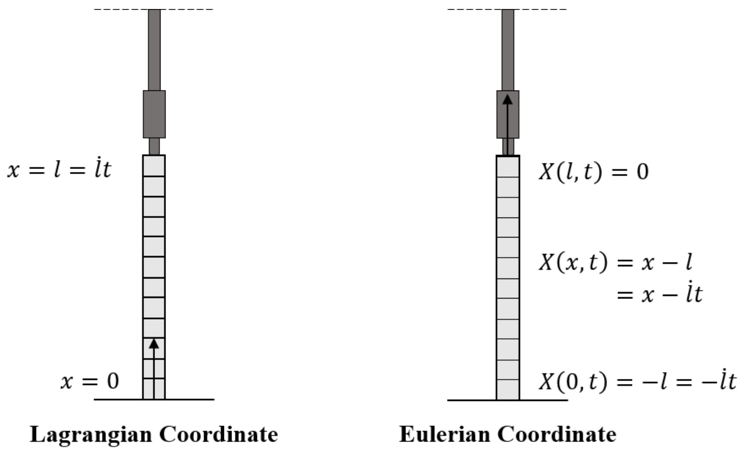

Figure 2-8 Lagrangian coordinate system and Eulerian coordinate system

2.3 Cylindrical Column Model

2.3.1 Theoretical background

To confirm the global buckling failure, consider the cylindrical structure with the constant cross-sectional area and the second moment of inertia in the length direction and the length l, as shown in the figure below. The bifurcation approach is used to find another equilibrium state assuming the deformed shape at the moment when buckling occurs. Since this buckling behavior generally occurs in the column member, it is called the column model. The body force applied to unit length is calculated as $q = \rho g A$, where ρ is the density of the material, g is the acceleration of gravity, and A is the cross-sectional area of the structure. The horizontal deflection $w(x)$ represents a displacement generated in the y direction at the location x. The equilibrium equation can be derived at the specific location by placing the moment and the internal moment generated by self-weight as equal [6]. In the equation, the modulus of elasticity E is described as $E = E_*(x)$, since it varies with time and is not uniform with location. Therefore, the governing equation for the global buckling of the 3D printed cylindrical structure can be expressed by substituting an equation representing the increasing dead weight of the structure and the stiffness of the material into the equilibrium equation.

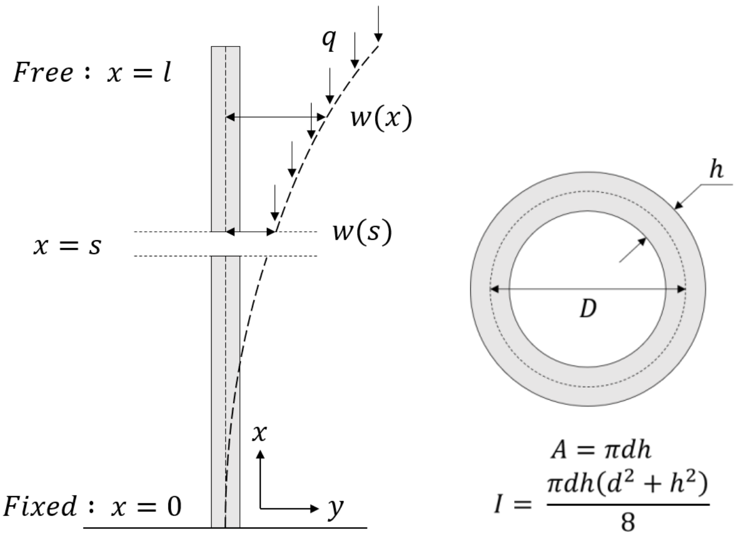

Figure 2-9 Free body diagram of column model to derive governing equation

2.3.2 Derivation of governing equation

The moment equation generated by the load acting on the deformed structure at a specific location $x = s$ can be described as follows

$$M(s) = \int_0^l q\big(w(x) - w(s)\big)dx \tag{2.1}$$

meanwhile, the internal moment at the same location can be expressed as Eq. (2.2) along the Euler - Bernoulli beam theory.

$$M_{int}(s) = E_* I \frac{d^2 w(s)}{ds^2} \tag{2.2}$$

The bending stiffness of the hollow cross-sectional cylinder is equal to the elastic modulus E_* multiplied by the second moment of interia I. Since the stiffness modulus is a function of height, the bending stiffness is also not constant along the lenghth.

$$E_* I = \frac{\pi h d\left(h^2 + D^2\right)}{8} E_*(x) = D_*(x) \tag{2.3}$$

here, d represents the average diameter between outer and inner circular and h is the height of layer. The moment equilibrium at location $x = s$ can be expressed as the following equation.

$$M_{int}(s) = M(s) \tag{2.4}$$

$$D_* \frac{d^2 w(s)}{ds^2} = \int_0^l q\big(w(x) - w(s)\big)dx \tag{2.5}$$

The buckling equation for the cylindrical structure subjected to the self-weight with the non-uniform elastic modulus in the length direction can be obtained by differentiating both sides with respect to s, as Eq. (2.6)

$$\frac{dD_*}{ds}\frac{d^2w(s)}{ds^2}+D_*\frac{d^3w(s)}{ds^3}=q(s-l)\frac{dw(s)}{ds} \tag{2.6}$$

The effect of increasing the elastic modulus of the material located at $x = 0$ over time can be expressed as below.

$$E_*(x=0,t)=g_*(t)E_0 \tag{2.7}$$

$$Linear\ function: g_*(t)=1+\xi_E t \tag{2.8}$$

Here, E_0 is the initial elastic modulus of the material discharged from the nozzle, and $g_*(t)$ is a function defining the curing effect. In this study, the stiffness modulus is assumed as a material that linearly increases. ξ_E represents the curing rate for the elastic modulus.

In Chapter 2.2.1, it is assumed that the length of the structure during construction increases to the constant speed $\dot{l}$. Parameter $\dot{l}$ is determined by the printing variables, and when the structure length is divided by the growth speed of length, the time t which represents consumed time is determined.

$$\dot{l}=\frac{Q}{v_n h T_l} \tag{2.9}$$

$$t=\frac{l}{\dot{l}} \tag{2.10}$$

where Q represents the volume of the material discharged per unit time, v_n represents the printing speed of nozzle and T_l is the printing period of a layer.

For convenience in calculation, the buckling equation consisting of variables x and t can be reformulated in terms of the Eulerian coordinate, X. In addition, the dimensionless Eulerian coordinate, $\bar{X},$ is defined as follows

$$X = X(x,t) = x - l = x - \dot{l}t \tag{2.11}$$

$$\bar{X}(x,t) = \frac{\xi_E X}{\dot{l}} = \frac{\xi_E}{\dot{l}}(x - l) = \frac{\xi_E}{\dot{l}}(x - \dot{l}t) \tag{2.12}$$

If the elastic modulus and curing function are expressed with the dimensionless coordinate system, it is as below

$$E_*(x,t) = \left[1 + \xi_E\left(t - \frac{x}{\dot{l}}\right)\right]E_0 \tag{2.13}$$

$$\bar{E}_*(\bar{X}) = \bar{g}_*(\bar{X})E_0 = (1 - \bar{X})E_0 \tag{2.14}$$

In order to make Eq. (2.6) dimensionless, a process of substituting x to $\bar{X}$ is necessary. Therefore, the following equation shows the relationship between differential of x and differential of $\bar{X}$.

$$x = \frac{\dot{l}}{\xi_E}\bar{X} + l \tag{2.15}$$

$$dx = \frac{\dot{l}}{\xi_E}d\bar{X} \tag{2.16}$$

Substitue Eq. (2.16) into Eq. (2.6)

$$L.H.S: \frac{dD_*}{dx}\frac{d^2w(x)}{dx^2} + D_*\frac{d^3w(x)}{dx^3} \tag{2.17}$$

$$= \left(\frac{\xi_E}{\dot{l}}\right)^3 \frac{d\bar{D}_*}{d\bar{X}} \frac{d^2 w\left(\bar{X}\right)}{d\bar{X}^2} + \left(\frac{\xi_E}{\dot{l}}\right)^3 \bar{D}_* \frac{d^3 w\left(\bar{X}\right)}{d\bar{X}^3}$$

$$R.H.S: q\left(x-l\right)\frac{dw\left(x\right)}{dx} = q\bar{X}\left(\frac{\dot{l}}{\xi_E}\right)\left(\frac{\xi_E}{\dot{l}}\right)\frac{dw\left(\bar{X}\right)}{d\bar{X}} \tag{2.18}$$

The horizontal deflection w is divided by the layer height h to represent the dimensionless deflection $\bar{w}$, and is applied to the buckling equation.

$$\left(\frac{\xi_E}{\dot{l}}\right)^3 \bar{D}_* \frac{d^3\bar{w}}{d\bar{X}^3} + \left(\frac{\xi_E}{\dot{l}}\right)^3 \frac{d\bar{D}_*}{d\bar{X}} \frac{d^2\bar{w}}{d\bar{X}^2} - q\bar{X}\frac{d\bar{w}}{d\bar{X}} = 0 \tag{2.19}$$

$$\bar{D}_* = \bar{D}_*\left(\bar{X}\right) = \bar{E}_*\left(\bar{X}\right)I = \bar{g}_*\left(\bar{X}\right)E_0 I = \bar{g}_*\left(\bar{X}\right)D_0 \tag{2.20}$$

Finally, the dimensionless buckling equation can be summarized by dividing Eq. (2.19) by $D_0\left(\frac{\xi_E}{\dot{l}}\right)^3$. Here, the initial bending stiffness can be expressed as $D_0 = \frac{\pi dh(d^2+h^2)}{8}E_0$.

$$\bar{g}_* \frac{d^3\bar{w}}{d\bar{X}^3} + \frac{d\bar{g}_*}{d\bar{X}} \frac{d^2\bar{w}}{d\bar{X}^2} - \lambda_c \bar{X}\frac{d\bar{w}}{d\bar{X}} = 0 \tag{2.21}$$

$$\lambda_c = \frac{q}{D_0}\left(\frac{\dot{l}}{\xi_E}\right)^3 = \frac{\rho g A}{D_0}\left(\frac{\dot{l}}{\xi_E}\right)^3, \quad A = \pi dh \tag{2.22}$$

The location $x = 0, l$ correspond to $\bar{X} = -\kappa, 0$ and are fixed end and free end, respectively. These boundary conditions are represented for the dimensionless Eulerian coordinate system $\bar{X}$.

$$\kappa = \frac{\xi_E l}{\dot{l}} \tag{2.23}$$

$$\begin{aligned}&Fixed\,at\,x=0,\bar{X}=-\kappa:\bar{w}=0,\frac{d\bar{w}}{d\bar{X}}=0\\&Free\,at\,x=l,\bar{X}=0:\frac{d^2\bar{w}}{d\bar{X}^2}=0,\frac{d^3\bar{w}}{d\bar{X}^3}=0\end{aligned}\tag{2.24}$$

The deflection w is assumed in the form of a polynomial as follows, since the integral caclus becomes simpler compared to the trigonometric function.

$$\bar{w}\left(\bar{X}\right)=\sum_{i=0}^{m}\bar{w}_i=\sum_{i=0}^{m}C_i\bar{X}^{i-1}=C_1+C_2\bar{X}+C_3\bar{X}^2+\cdots+C_m\bar{X}^{m-1}\tag{2.25}$$

here, m represents the degree of the polynomial and C_m is the m^{th} unknown coefficient. In this paper, $m=8$ is used. Substituting the boundary conditions from Eq. (2.24), the four coefficients are first found.

$$\begin{aligned}C_1&=3C_5\kappa^4-4C_6\kappa^5+5C_7\kappa^6-6C_8\kappa^7\\C_2&=4C_5\kappa^3-5C_6\kappa^4+6C_7\kappa^5-7C_8\kappa^6\\C_3&=C_4=0\end{aligned}\tag{2.26}$$

By substituting Eq. (2.26) into Eq. (2.25), it becomes a trial function satisfying the boundary condition. This is expressed as a linear combination of the unknown coefficient C_m and the basis function as shown in Eq. (2.27)

$$\begin{aligned}\bar{w}_{m(=5,6,\cdots)}\left(\bar{X}\right)=&\left(3C_5\kappa^4-4C_6\kappa^5+5C_7\kappa^6-6C_8\kappa^7\right)\\&+\left(4C_5\kappa^3-5C_6\kappa^4+6C_7\kappa^5-7C_8\kappa^6\right)\bar{X}\\&+C_5\bar{X}^4+C_6\bar{X}^5+C_7\bar{X}^6+C_8\bar{X}^7\end{aligned}\tag{2.27}$$

The solution of the differential Eq. (2.21) is calculated from the weak form as shown in Eq. (2.29) below. The approximate solution can be obtained by using the weighted residual method, which is a way to make the weighed mean of the error zero.

$$\int_{\bar{X}=-\kappa}^{\bar{X}=0} (\bar{R}\delta\bar{w}_m)d\bar{X} = 0 \tag{2.28}$$

$$\begin{gathered} \bar{R}\left(\bar{X}\right) = \bar{g}_* \frac{d^3\bar{w}_m}{d\bar{X}^3} + \frac{d\bar{g}_*}{d\bar{X}}\frac{d^2\bar{w}_m}{d\bar{X}^2} - \lambda_c \bar{X}\frac{d\bar{w}_m}{d\bar{X}} \\ \delta\bar{w}_m = \frac{\partial\bar{w}_m}{\partial C_m}\delta C_m \end{gathered} \tag{2.29}$$

The residual is constructed by substituting the trial function into the left-hand side of Eq. (2.21), and partial differentiation is performed for each unknown coefficient to obtain the weight function consisting of κ and $\bar{X}$. By calculating Eq. (2.28), a linear equation of the unknown coefficient can be obtained. Then, by constructing this as a matrix equation for the unknown coefficient, the buckling equation is organized as an eigenvalue problem.

$$\begin{gathered} \begin{bmatrix} A_{5,5} & \cdots & A_{5,m} \\ \vdots & \ddots & \vdots \\ A_{m,1} & \cdots & A_{m,m} \end{bmatrix} \cdot \begin{bmatrix} C_5 \\ \vdots \\ C_m \end{bmatrix} = \begin{bmatrix} 0 \\ \vdots \\ 0 \end{bmatrix} \\ Non-trivial\ solution : \det\left|A\right| = 0 \end{gathered} \tag{2.30}$$

The high-order equation obtained by calculating the determinant of matrix is an equation in terms of λ_c and κ, and can be analyzed by introducing the following two dimensionless parameters.

$$\bar{l}_{cr,column} = \lambda_c^{1/3}\kappa = \left(\frac{\rho g A}{D_0}\right)^{\frac{1}{3}} l_{cr}$$
$$\bar{\xi}_{E,column} = \lambda_c^{-1/3} = \left(\frac{D_0}{\rho g A}\right)^{\frac{1}{3}}\left(\frac{\xi_E}{\dot{l}}\right) \tag{2.31}$$

Here, $\bar{l}_{cr}$ is the non-dimensional buckling length including the body force and bending stiffness, and $\bar{\xi}_E$ is the non-dimensional curing rate representing the ratio of the vertical printing speed to the curing rate. Finally, $\bar{l}_{cr}$, which is a solution of the dimensionless high-order buckling equation, is obtained from the value of $\bar{\xi}_E$.

2.4 Cylindrical Shell Model

2.4.1 Principle of total potential energy

When the buckling occurs, deformation occurs in the cross section, and if it is not constant in the length direction, it is considred as local buckling. These behaviors are analyzed by using the minimum total potential energy in the shell element. The total potential enegy consists of the elastic strain energy and the potential energy and is expresses as a sum. The strain energy consists of two parts, thebending strain energy and the membrane strain energy due to the stretching of the mid-surface. The following strain energy equation can be obtained from 'Theory of Elastic Stability' written by Timoshenko and Gere [8].

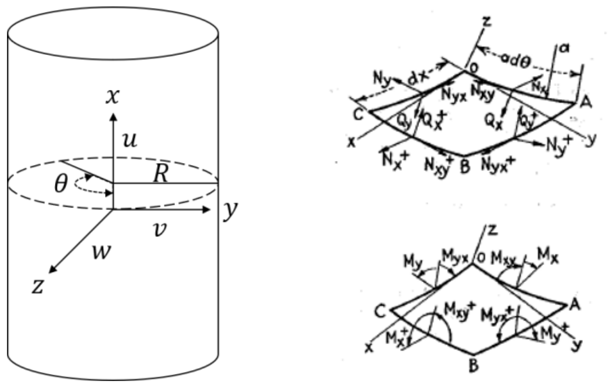

Figure 2-10 (a) The coordinates in the middle surface of the shell, (b) The element cut out from the cylindrical shell (from Timoshenko et. al., 1963)

The strain energy due to bending and twisting moments of thin plate is expressed by integration as below

$$
\begin{aligned}
U_b = \frac{1}{2}\iint D\Bigg[&\left\{\left(\frac{\partial^2 w}{\partial x^2}\right)^2 + \left(\frac{\partial^2 w}{\partial y^2}\right)^2 + 2\nu\frac{\partial^2 w}{\partial x^2}\frac{\partial^2 w}{\partial y^2}\right\} \\
&+\left\{2(1-\nu)\left(\frac{\partial^2 w}{\partial x \partial y}\right)^2\right\}\Bigg]dA
\end{aligned}
\tag{2.32}
$$

in which D is the flexural rigidity given by

$$D = \frac{E}{1-\nu^2}\int_{-h/2}^{h/2} z^2 dz = \frac{Eh^3}{12\left(1-\nu^2\right)} \tag{2.33}$$

where ν is Possion's ratio.

The part of the strain energy due to stretching of the middle surface of thin plate is

$$U_s = \frac{1}{2}\iint\left(N_x\varepsilon_1 + N_y\varepsilon_2 + N_{xy}\gamma\right)dA \tag{2.34}$$

whereby the normal forces applied at the centroid of the side of the element are given by

$$
\begin{gathered}
N_x = \frac{Eh}{1-\nu^2}\left(\varepsilon_1 + \nu\varepsilon_2\right), \qquad N_y = \frac{Eh}{1-\nu^2}\left(\varepsilon_2 + \nu\varepsilon_1\right) \\
N_{xy} = \frac{\gamma h E}{2(1+\nu)}
\end{gathered}
\tag{2.35}
$$

with the components of strain $\varepsilon_1, \varepsilon_2$ and γ of the middle surface of element.

Substituting in Eq. (2.32) the changes of curvatures χ_x, χ_θ and $\chi_{x\theta}$ instead of curvatures $\frac{\partial^2 w}{\partial x^2}$, $\frac{\partial^2 w}{\partial y^2}$ and $\frac{\partial^2 w}{\partial x \partial y}$ to consider the circular cylindrical shell instead of the thin plate, Eq. (2.32) will be written as follows

$$U_b = \frac{1}{2}\int_0^l \int_0^{2\pi} D_* \left[{\chi_x}^2 + {\chi_\theta}^2 + 2\nu \chi_x \chi_\theta + 2(1-\nu){\chi_{x\theta}}^2 \right] R d\theta dx \quad (2.36)$$

where R is the radius of the middle surface of the shell and D_* is the heterogeneous flexural rigidity which is considering the curing effect of the material given by

$$D_*(x) = \frac{E_*(x)}{1-\nu^2}\int_{-h/2}^{h/2} z^2 dz = \frac{E_*(x) h^3}{12(1-\nu^2)}. \quad (2.37)$$

where E_* is the heterogenous stiffness modulus with the linear curing function as Eq. (2.8).

Eq. (2.34) will be expressed as below in terms of the strain ε_x, ε_θ and $\varepsilon_{x\theta}$

$$U_s = \frac{h}{2(1-\nu^2)}\int_0^l \int_0^{2\pi} E_* \left[\varepsilon_x^2 + \varepsilon_\theta^2 + 2\nu \varepsilon_x \varepsilon_\theta + \frac{(1-\nu)}{2}\varepsilon_{x\theta}^2 \right] R d\theta dx \quad (2.38)$$

The total energy of deformation is obtained by adding together expression (2.36) and (2.38) which are expressed with the three curvature changes and the three strain componenets, respectively. These components are represented in terms of the displacements u, v and w as follows

$$\varepsilon_x = \frac{\partial u}{\partial x}, \quad \varepsilon_\theta = \frac{1}{R}\left(\frac{\partial v}{\partial \theta} + w \right), \quad \gamma = \frac{1}{R}\frac{\partial u}{\partial \theta} + \frac{\partial v}{\partial x} \quad (2.39)$$

$$\chi_x = -\frac{\partial^2 w}{\partial x^2}, \quad \chi_\theta = \frac{1}{R^2}\left(\frac{\partial v}{\partial \theta} - \frac{\partial^2 w}{\partial \theta^2}\right)$$

$$\chi_{x\theta} = \frac{1}{R}\left(\frac{\partial v}{\partial x} - \frac{\partial^2 w}{\partial x \partial \theta}\right)$$

The potential energy generated by the in-plane forces can be expressed as

$$V = \frac{1}{2}\int_0^l \int_0^{2\pi} \eta_{xx}\left[\left(\frac{\partial v}{\partial x}\right)^2 + \left(\frac{\partial w}{\partial x}\right)^2\right] R d\theta dx \tag{2.40}$$

where η_{xx} denotes the compressive self-weight subjecting to the opposite direction of x-axis. The potential energy V is rewritten as

$$V = -\frac{1}{2}\int_0^l \int_0^{2\pi} \rho g h (l - x)\left[\left(\frac{\partial v}{\partial x}\right)^2 + \left(\frac{\partial w}{\partial x}\right)^2\right] R d\theta dx \tag{2.41}$$

Thus, the total potential energy of the circular cylindrical shell can be expressed by adding together all of the strain energy and the potential energy.

$$\mathit{Total\ Potential\ Energy} : \Pi = U_b + U_s + V \tag{2.42}$$

2.4.2 Displacement Approxiamtion Function

The dimesionless deflection is specified as following expressions which are dividing displacement u, v and w by layer height, h.

$$\bar{u}(x)=\frac{u(x)}{h}, \quad \bar{v}(x)=\frac{v(x)}{h}, \quad \bar{w}(x)=\frac{w(x)}{h} \tag{2.43}$$

Since the sinusoidal buckling wave is expected to form in the circumferential direction of the cylindrical shell, the displacements are the functions of variables x and θ and they may be separated as below [7]

$$\begin{aligned} u(x,\theta)&=u(x)\cos(n\theta)=h\bar{u}(x)\cos(n\theta) \\ v(x,\theta)&=v(x)\sin(n\theta)=h\bar{v}(x)\sin(n\theta) \\ w(x,\theta)&=w(x)\cos(n\theta)=h\bar{w}(x)\cos(n\theta) \end{aligned} \tag{2.44}$$

where n is the circumferential wavenumber which is an integer greater than or equal to zero, $n = 0,1,2,\cdots$. If $n = 0$, Eq. (2.44) represents axisymmetric buckling, otherwise it provides axi-unsymmetric buckling modes.

Eq. (2.44) can be rewritten in terms of dimensionless coordinate which is already dealt from Chaper 2.3 Eq. (2.12) and will also be covred in Eq. (2.49).

$$\begin{aligned} u(x,\theta)&=u(x)\cos(n\theta),\ u(\bar{X},\theta)=h\bar{u}(\bar{X})\cos(n\theta) \\ v(x,\theta)&=v(x)\sin(n\theta),\ v(\bar{X},\theta)=h\bar{v}(\bar{X})\sin(n\theta) \\ w(x,\theta)&=w(x)\cos(n\theta),\ w(\bar{X},\theta)=h\bar{w}(\bar{X})\cos(n\theta) \end{aligned} \tag{2.45}$$

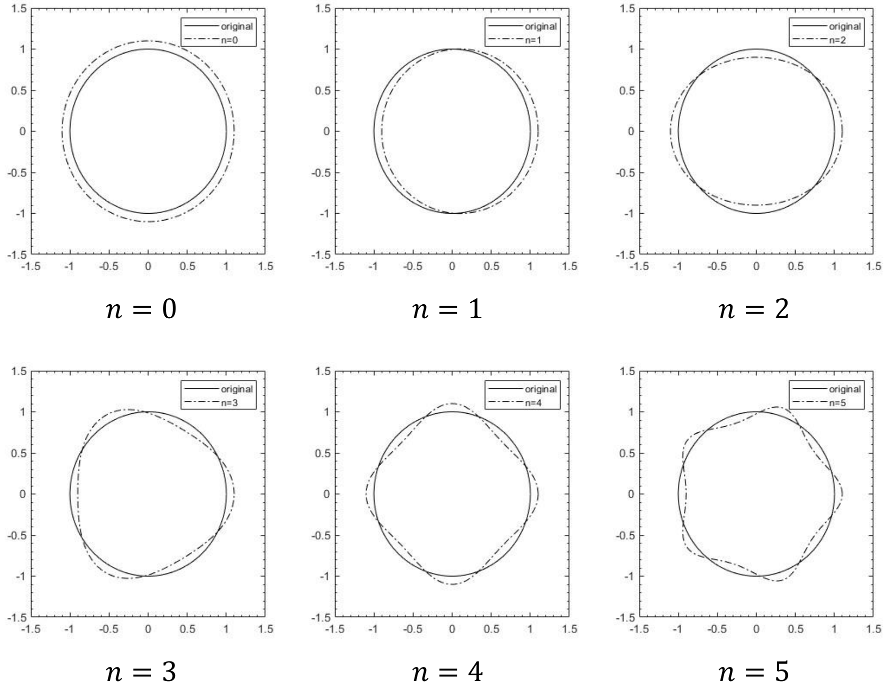

Figure 2-11 Deformed cross-section according to the wavenumber n = 0 ~ 5

To approximate the dimensionless displacements $\bar{u}$, $\bar{v}$ and $\bar{w}$, the p-version finite element method suggested by Babuska is adopted. The admissible functions can be expressed by using polynomial functions as follows

$$
\begin{aligned}
&\bar{u}\left(\bar{X}\right) = f_u\left(\bar{X}\right)\sum_{i=1}^{k} C_i^u \bar{X}^{i-1}, \quad f_u\left(\bar{X}\right) = \left(\bar{X} + \kappa\right)^{\Gamma_b^u} \bar{X}^{\Gamma_t^u} \\
&\bar{v}\left(\bar{X}\right) = f_v\left(\bar{X}\right)\sum_{i=1}^{p} C_i^v \bar{X}^{i-1}, \quad f_v\left(\bar{X}\right) = \left(\bar{X} + \kappa\right)^{\Gamma_b^v} \bar{X}^{\Gamma_t^v} \\
&\bar{w}\left(\bar{X}\right) = f_w\left(\bar{X}\right)\sum_{i=1}^{q} C_i^w \bar{X}^{i-1}, \quad f_w\left(\bar{X}\right) = \left(\bar{X} + \kappa\right)^{\Gamma_b^w} \bar{X}^{\Gamma_t^w}
\end{aligned}
\tag{2.46}
$$

where C_i^u, C_i^v and C_i^w are coefficients of the admissible functions and k, p and q are the number of polynomial terms. To satisfy the geometric boundary conditions of the cylindrical shell, the power terms of the basic functions $f_u(\bar{X})$, $f_v(\bar{X})$ and $f_w(\bar{X})$ are determined by the following equations.

$$\begin{gathered} Free: \Gamma_j^u = 0, \Gamma_j^v = 0, \Gamma_j^w = 0 \\ Simply\,Supported: \Gamma_j^u = 0, \Gamma_j^v = 1, \Gamma_j^w = 1 \\ Clamped: \Gamma_j^u = 1, \Gamma_j^v = 1, \Gamma_j^w = 2 \end{gathered} \tag{2.47}$$

where j indicates bottom or top. In this paper, since the cylindrical shell which has clamped bottom and free top is considered, substituting the corresponding factor to Eq. (2.47) and the number of polynomial terms as $k = p = q = 8$, the approximated displacement functions are expressed as follows

$$\begin{gathered} \bar{u}\left(\bar{X}\right) = \left(\bar{X} + \kappa\right)\sum_{i=1}^{8} C_i^u \bar{X}^{i-1} \\ \bar{v}\left(\bar{X}\right) = \left(\bar{X} + \kappa\right)\sum_{i=1}^{8} C_i^v \bar{X}^{i-1} \\ \bar{w}\left(\bar{X}\right) = \left(\bar{X} + \kappa\right)^2 \sum_{i=1}^{8} C_i^w \bar{X}^{i-1} \end{gathered} \tag{2.48}$$

2.4.3 Derivation of dimensionless expression of total potential energy

In the same manner as deriving the dimensionless column buckling equation from previous chapter 2.3, the dimensionless coordinate system $\bar{X}$ is used instead of Lagrangian coordinate system.

$$\bar{X} = \frac{\xi_E X}{\dot{l}} = \frac{\xi_E}{\dot{l}}(x - l) = \frac{\xi_E}{\dot{l}}\left(x - \dot{l}t\right) \tag{2.49}$$

The expression of bending strain energy (2.36) can be rewritten as Eq. (2.50) in terms of the displacements u, v and w.

$$\begin{aligned} U_b = \frac{1}{2}\int_0^l \int_0^{2\pi} D_* \Bigg[& \left(-\frac{\partial^2 w}{\partial x^2}\right)^2 + \frac{1}{R^4}\left(\frac{\partial v}{\partial \theta} - \frac{\partial^2 w}{\partial \theta^2}\right)^2 \\ & + \frac{2\nu}{R^2}\left(-\frac{\partial^2 w}{\partial x^2}\right)\left(\frac{\partial v}{\partial \theta} - \frac{\partial^2 w}{\partial \theta^2}\right) \\ & + \frac{2(1-\nu)}{R^2}\left(\frac{\partial v}{\partial x} - \frac{\partial^2 w}{\partial x \partial \theta}\right)^2 \Bigg] R d\theta dx \end{aligned} \tag{2.50}$$

Substituting Eqs. (2.37), (2.45) and (2.49), the bending strain energy with diensionless coordinate system is expressed as follows

$$\begin{aligned} U_b = \frac{E_0 h^3}{24(1-\nu^2)} \int_{-\kappa}^{0} \int_0^{2\pi} (1-\bar{X}) \Bigg[& h^2 \frac{\xi_E{}^4}{\dot{l}^4} \cos^2 n\theta \left(\frac{\partial^2 \bar{w}}{\partial \bar{X}^2}\right)^2 \\ & + \frac{h^2}{R^4} n^2 \cos^2 n\theta \left\{\bar{v}(\bar{X}) + n\bar{w}(\bar{X})\right\}^2 \\ & - \frac{2\nu h^2}{R^2} \frac{\xi_E{}^2}{\dot{l}^2} n \cos^2 n\theta \left(\frac{\partial^2 \bar{w}}{\partial \bar{X}^2}\right)\left\{\bar{v}(\bar{X}) + n\bar{w}(\bar{X})\right\} \\ & + \frac{2(1-\nu)h^2}{R^2} \frac{\xi_E{}^2}{\dot{l}^2} \sin^2 n\theta \left(\frac{\partial \bar{v}}{\partial \bar{X}} + n\frac{\partial \bar{w}}{\partial \bar{X}}\right)^2 \Bigg] R d\theta \left(\frac{\dot{l}}{\xi_E} d\bar{X}\right) \end{aligned} \tag{2.51}$$

where κ is non-dimensional location of the bottom and $\kappa = \xi_E l/\dot{l}$.

To make the equation simple, take $h^2 R \frac{{\xi_E}^3}{\dot{l}^3}$ out of the integral and use D_0 expression instead of $E_0 h^3/12(1-\nu^2)$.

$$
\begin{aligned}
U_b = \frac{D_0}{2} h^2 R \frac{{\xi_E}^3}{\dot{l}^3} \int_{-\kappa}^{0} \int_{0}^{2\pi} \left(1-\bar{X}\right) & \left[\cos^2 n\theta \left(\frac{\partial^2 \bar{w}}{\partial \bar{X}^2} \right)^2 \right. \\
& + \frac{1}{R^4} \frac{\dot{l}^4}{{\xi_E}^4} n^2 \cos^2 n\theta \left\{ \bar{v}\left(\bar{X}\right) + n\bar{w}\left(\bar{X}\right) \right\}^2 \\
& - \frac{2\nu}{R^2} \frac{\dot{l}^2}{{\xi_E}^2} n \cos^2 n\theta \left(\frac{\partial^2 \bar{w}}{\partial \bar{X}^2} \right) \left\{ \bar{v}\left(\bar{X}\right) + n\bar{w}\left(\bar{X}\right) \right\} \\
& \left. + \frac{2(1-\nu)}{R^2} \frac{\dot{l}^2}{{\xi_E}^2} \sin^2 n\theta \left(\frac{\partial \bar{v}}{\partial \bar{X}} + n \frac{\partial \bar{w}}{\partial \bar{X}} \right)^2 \right] d\theta d\bar{X}
\end{aligned}
\tag{2.52}
$$

Finally, using dimensionless parameter, $\varepsilon = \frac{\xi_E}{\dot{l}} R$, can reduce the number of parameters in the equation and makes the calculation time faster.

$$
\begin{aligned}
U_b = \frac{D_0}{2} h^2 R \frac{{\xi_E}^3}{\dot{l}^3} \int_{-\kappa}^{0} \int_{0}^{2\pi} \left(1-\bar{X}\right) & \left[\cos^2 n\theta \left(\frac{\partial^2 \bar{w}}{\partial \bar{X}^2} \right)^2 \right. \\
& + \frac{1}{\varepsilon^4} n^2 \cos^2 n\theta \left\{ \bar{v}\left(\bar{X}\right) + n\bar{w}\left(\bar{X}\right) \right\}^2 \\
& - \frac{2\nu}{\varepsilon^2} n \cos^2 n\theta \left(\frac{\partial^2 \bar{w}}{\partial \bar{X}^2} \right) \left\{ \bar{v}\left(\bar{X}\right) + n\bar{w}\left(\bar{X}\right) \right\} \\
& \left. + \frac{2(1-\nu)}{\varepsilon^2} \sin^2 n\theta \left(\frac{\partial \bar{v}}{\partial \bar{X}} + n \frac{\partial \bar{w}}{\partial \bar{X}} \right)^2 \right] d\theta d\bar{X}
\end{aligned}
\tag{2.53}
$$

The membrane strain energy and the potential energy can be reformulated with the same process as Eq. (2.50) ~ (2.52).

$$U_s = \frac{h}{2\left(1-\nu^2\right)}\int_0^l \int_0^{2\pi} E_* \left[\left(\frac{\partial u}{\partial x}\right)^2 + \frac{1}{R^2}\left(\frac{\partial v}{\partial \theta} + w\right)^2 \right.$$
$$\left. + \frac{2\nu}{R}\left(\frac{\partial u}{\partial x}\right)\left(\frac{\partial v}{\partial \theta} + w\right) + \frac{\left(1-\nu\right)}{2}\left(\frac{1}{R}\frac{\partial u}{\partial \theta} + \frac{\partial v}{\partial x}\right)^2\right] R d\theta dx \tag{2.54}$$

where the heterogeneous elastic modulus is represented as $E_* = E_0(1-\bar{X})$. Substituting Eqs. (2.37), (2.45) and (2.49) in Eq. (2.54), the membrane strain energy is expressed as follows

$$U_s = \frac{E_0 h}{2\left(1-\nu^2\right)}\int_{-\kappa}^0 \int_0^{2\pi} \left(1-\bar{X}\right)\left[h^2 \frac{\xi_E{}^2}{\dot{l}^2}\cos^2 n\theta \left(\frac{\partial \bar{u}}{\partial \bar{X}}\right)^2 \right.$$
$$+ \frac{h^2}{R^2}\cos^2 n\theta \left\{n\bar{v}\left(\bar{X}\right) + \bar{w}\left(\bar{X}\right)\right\}^2$$
$$+ 2\nu \frac{h^2}{R}\frac{\xi_E}{\dot{l}}\cos^2 n\theta \left(\frac{\partial \bar{u}}{\partial \bar{X}}\right)\left\{n\bar{v}\left(\bar{X}\right) + \bar{w}\left(\bar{X}\right)\right\}$$
$$\left. + \frac{\left(1-\nu\right)}{2} h^2 \frac{\xi_E{}^2}{\dot{l}^2}\sin^2 n\theta \left(\frac{\partial \bar{v}}{\partial \bar{X}} - \frac{n}{R}\frac{\dot{l}}{\xi_E}\bar{u}\left(\bar{X}\right)\right)^2\right] R\frac{\dot{l}}{\xi_E} d\theta d\bar{X} \tag{2.55}$$

Take $h^2 R \frac{\xi_E}{\dot{l}}$ out of the integral and substitue D_0.

$$U_s = \frac{6D_0}{h^2} h^2 R \frac{\xi_E}{\dot{l}} \int_{-\kappa}^0 \int_0^{2\pi} \left(1-\bar{X}\right)\left[\cos^2 n\theta \left(\frac{\partial \bar{u}}{\partial \bar{X}}\right)^2 \right.$$
$$+ \frac{1}{R^2}\frac{\dot{l}^2}{\xi_E{}^2}\cos^2 n\theta \left\{n\bar{v}\left(\bar{X}\right) + \bar{w}\left(\bar{X}\right)\right\}^2$$
$$+ 2\nu \frac{1}{R}\frac{\dot{l}}{\xi_E}\cos^2 n\theta \left(\frac{\partial \bar{u}}{\partial \bar{X}}\right)\left\{n\bar{v}\left(\bar{X}\right) + \bar{w}\left(\bar{X}\right)\right\}$$
$$\left. + \frac{\left(1-\nu\right)}{2}\sin^2 n\theta \left(\frac{\partial \bar{v}}{\partial \bar{X}} - \frac{n}{R}\frac{\dot{l}}{\xi_E}\bar{u}\left(\bar{X}\right)\right)^2\right] d\theta d\bar{X} \tag{2.56}$$

Final expression of the membrane strain energy with parameter, ε, is derived.

$$
\begin{aligned}
U_s = 6D_0 R \frac{\xi_E}{l} \int_{-\kappa}^{0} \int_{0}^{2\pi} \left(1-\bar{X}\right) \Bigg[& \cos^2 n\theta \left(\frac{\partial \bar{u}}{\partial \bar{X}}\right)^2 \\
& + \frac{1}{\varepsilon^2} \cos^2 n\theta \left\{ n\bar{v}\left(\bar{X}\right) + \bar{w}\left(\bar{X}\right) \right\}^2 \\
& + 2\nu \frac{1}{\varepsilon} \cos^2 n\theta \left(\frac{\partial \bar{u}}{\partial \bar{X}}\right) \left\{ n\bar{v}\left(\bar{X}\right) + \bar{w}\left(\bar{X}\right) \right\} \\
& + \frac{\left(1-\nu\right)}{2} \sin^2 n\theta \left(\frac{\partial \bar{v}}{\partial \bar{X}} - n\varepsilon \bar{u}\left(\bar{X}\right)\right)^2 \Bigg] d\theta d\bar{X}
\end{aligned}
\tag{2.57}
$$

Using Eqs. (2.45) and (2.49), the potential energy Eq. (2.41) is rewritten as follows

$$
\begin{aligned}
V = \frac{\rho g h}{2} \frac{l}{\xi_E} \int_{-\kappa}^{0} \int_{0}^{2\pi} \bar{X} \Bigg[& h^2 \frac{\xi_E^{\ 2}}{l^2} sin^2 n\theta \left(\frac{\partial \bar{v}}{\partial \bar{X}}\right)^2 \\
& + h^2 \frac{\xi_E^{\ 2}}{l^2} cos^2 n\theta \left(\frac{\partial \bar{w}}{\partial \bar{X}}\right)^2 \Bigg] R \frac{l}{\xi_E} d\theta d\bar{X}
\end{aligned}
\tag{2.58}
$$

By taking $h^2 R \frac{\xi_E}{l}$ out of the integral, final expression of the potential energy is obtained.

$$
\begin{aligned}
V = \frac{\rho g h^3}{2} R \int_{-\kappa}^{0} \int_{0}^{2\pi} \bar{X} \Bigg[& sin^2 n\theta \left(\frac{\partial \bar{v}}{\partial \bar{X}}\right)^2 \\
& + cos^2 n\theta \left(\frac{\partial \bar{w}}{\partial \bar{X}}\right)^2 \Bigg] R \frac{l}{\xi_E} d\theta d\bar{X}
\end{aligned}
\tag{2.59}
$$

The total potential energy of the cylindrical shell can be formulated by adding Eqs. (2.53), (2.57) and (2.58). The terms which are multiplied in front of the integrals are organized and the common term, $\frac{D_0}{2} h^2 R \frac{\xi_E^{\ 3}}{l^3}$ can be taken out as following ways.

$$\frac{D_0}{2}h^2R\frac{\xi_E{}^3}{l^3}\rightarrow 1$$

$$6D_0R\frac{\xi_E}{l}\rightarrow\left(\frac{D_0}{2}h^2R\frac{\xi_E{}^3}{l^3}\right)\frac{12}{h^2}\frac{l^2}{\xi_E{}^2}\rightarrow 12\frac{1}{\alpha^2}\frac{1}{\epsilon^2} \tag{2.60}$$

$$\frac{\rho g h^3}{2}R\rightarrow\left(\frac{D_0}{2}h^2R\frac{\xi_E{}^3}{l^3}\right)\frac{\rho g h}{D_0}\frac{l^3}{\xi_E{}^3}\rightarrow\lambda_s$$

whereby dimensionless parameters for the shell model α and λ_s are given by

$$\alpha=\frac{h}{R} \tag{2.61}$$

$$\lambda_s=\frac{\rho g h}{D_0}\left(\frac{l}{\xi_E}\right)^3 \tag{2.62}$$

The differences between parameter λ_c and λ_s are that the layer height h is included in λ_s instead of the cross-sectional area A which is in λ_c and the expression of the initial bending stiffness is $D_{0,shell}=E_0h^3/12(1-\nu^2)$, otherwise $D_{0,column}=\frac{\pi d h(d^2+h^2)}{8}E_0$. The parameter α represents the ratio the layer height h of the raidus of the cylindrical shell h. Figure 2-12 shows the configuration of the cross-section of the shell.

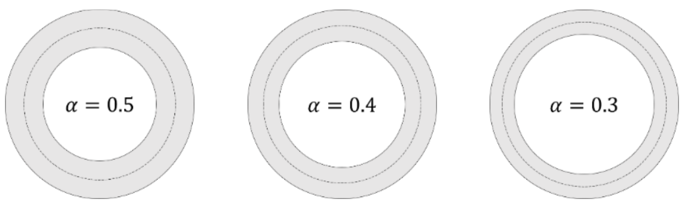

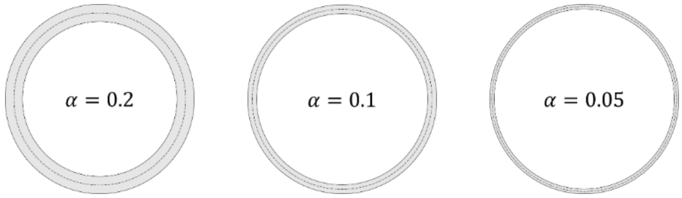

Figure 2-12 The configuration of the cross-section of the shell according to the different values of the parameter α

Finally, the total potential energy is expressed as below, Eq. (2.63).

$$
\begin{aligned}
\Pi = \left(\frac{D_0}{2} h^2 R \frac{\xi_E{}^3}{l^3}\right) \int_{-\kappa}^{0} \int_{0}^{2\pi} \left(1-\bar{X}\right) \Bigg[& \cos^2 n\theta \left(\frac{\partial^2 \bar{w}}{\partial \bar{X}^2}\right)^2 \\
& + \frac{1}{\varepsilon^4} n^2 \cos^2 n\theta \left\{\bar{v}\left(\bar{X}\right) + n\bar{w}\left(\bar{X}\right)\right\}^2 \\
& - \frac{2\nu}{\varepsilon^2} n \cos^2 n\theta \left(\frac{\partial^2 \bar{w}}{\partial \bar{X}^2}\right) \left\{\bar{v}\left(\bar{X}\right) + n\bar{w}\left(\bar{X}\right)\right\} \\
& + \frac{2(1-\nu)}{\varepsilon^2} \sin^2 n\theta \left(\frac{\partial \bar{v}}{\partial \bar{X}} + n \frac{\partial \bar{w}}{\partial \bar{X}}\right)^2 \Bigg] \\
& + 12 \frac{1}{\alpha^2} \frac{1}{\epsilon^2} \left(1-\bar{X}\right) \Bigg[\cos^2 n\theta \left(\frac{\partial \bar{u}}{\partial \bar{X}}\right)^2 \\
& + \frac{1}{\varepsilon^2} \cos^2 n\theta \left\{n\bar{v}\left(\bar{X}\right) + \bar{w}\left(\bar{X}\right)\right\}^2 \\
& + 2\nu \frac{1}{\varepsilon} \cos^2 n\theta \left(\frac{\partial \bar{u}}{\partial \bar{X}}\right) \left\{n\bar{v}\left(\bar{X}\right) + \bar{w}\left(\bar{X}\right)\right\} \\
& + \frac{(1-\nu)}{2} \sin^2 n\theta \left(\frac{\partial \bar{v}}{\partial \bar{X}} - n\varepsilon \bar{u}\left(\bar{X}\right)\right)^2 \Bigg] \\
& + \lambda_s \bar{X} \left[sin^2 n\theta \left(\frac{\partial \bar{v}}{\partial \bar{X}}\right)^2 + cos^2 n\theta \left(\frac{\partial \bar{w}}{\partial \bar{X}}\right)^2 \right] d\theta d\bar{X}
\end{aligned}
\tag{2.63}
$$

This expression consists of the five parameters, such as α, ε, λ, n and κ.

Substituting the approximated displacement functions from Eq. (2.48) in Eq.

(2.63), the total potential energy can be minimized by partial derivative with respect to undetermined coefficients C_i^u, C_i^v and C_i^w as following equation.

$$\frac{\partial \Pi}{\partial C_i^u} = \frac{\partial \Pi}{\partial C_i^v} = \frac{\partial \Pi}{\partial C_i^w} = 0, i = 1, 2, \ldots, (k, p, q) \tag{2.64}$$

Thus, an eigenvalue problem is obtained for an analysis of the local buckling behavior of the circular cylindrical shell.

$$\begin{bmatrix} A_{1,1} & \cdots & A_{1,k+p+q} \\ \vdots & \ddots & \vdots \\ A_{k+p+q,1} & \cdots & A_{k+p+q,k+p+q} \end{bmatrix} \cdot \begin{bmatrix} C_1^u \\ \vdots \\ C_k^u \\ C_1^v \\ \vdots \\ C_p^v \\ C_1^w \\ \vdots \\ C_q^w \end{bmatrix} = \begin{bmatrix} 0 \\ \vdots \\ 0 \end{bmatrix} \tag{2.65}$$

$$Non-trivial\,solution : \det|A| = 0$$

A high-order equation obtained from determination of matrix A can be rewritten in terms of three non-dimensional paramters $\bar{R}$, $\bar{\xi}_{E,shell}$ and $\bar{l}_{cr,shell}$.

$$\bar{l}_{cr,shell} = \lambda_s^{1/3}\kappa = \left(\frac{\rho g h}{D_0}\right)^{\frac{1}{3}} l_{cr} \tag{2.66}$$

$$\bar{R} = \lambda_s^{1/3}\epsilon = \left(\frac{\rho g h}{D_0}\right)^{\frac{1}{3}} R$$

$$\bar{\xi}_{E,shell} = \lambda_s^{-1/3} = \left(\frac{D_0}{\rho g h}\right)^{\frac{1}{3}} \left(\frac{\xi_E}{\dot{l}}\right)$$

where $\bar{R}$ and $\bar{\xi}_{E,shell}$ represents the dimensionless radius of the cylindrical shell and the dimensionless curing rate, respectively, and and $\bar{l}_{cr,shell}$ is the dimensionless critical buckling length. After the various values of α, n, $\bar{R}$ and $\bar{\xi}_{E,shell}$ are substituted in the governing equation, the dimensioless buckling length can be found.

2.5 Conversion Factor

Since the parameter λ has different form for column model and shell model as expressed in Eqs. (2.22) and (2.62), respectively, a conversion factor which is the ratio between λ_{shell} and λ_{column} is necessary to plot a graph comparing the two models. The factor K can be drived as follows

$$K=\frac{\bar{\xi}_{E,shell}}{\bar{\xi}_{E,column}}=\frac{\lambda_s^{-1/3}}{\lambda_c^{-1/3}}=\left(\frac{\lambda_c}{\lambda_s}\right)^{\frac{1}{3}}=\frac{\left(\dfrac{D_{0,shell}}{\rho gh}\right)^{\frac{1}{3}}\left(\dfrac{\xi_E}{\dot{l}}\right)}{\left(\dfrac{D_{0,column}}{\rho gA}\right)^{\frac{1}{3}}\left(\dfrac{\xi_E}{\dot{l}}\right)}$$

$$=\left(\frac{D_{0,shell}A}{D_{0,column}h}\right)^{\frac{1}{3}}=\left(\frac{\dfrac{E_0h^3}{12\left(1-\nu^2\right)}A}{\dfrac{E_0A\left(d^2+h^2\right)}{8}h}\right)^{\frac{1}{3}}=\left(\frac{2h^2}{3\left(1-\nu^2\right)\left(4R^2+h^2\right)}\right)^{\frac{1}{3}} \tag{2.67}$$

$$=\left(\frac{2}{3\left(1-\nu^2\right)\left(4\dfrac{R^2}{h^2}+1\right)}\right)^{\frac{1}{3}}=\left(\frac{2}{3\left(1-\nu^2\right)\left(\dfrac{4}{\alpha^2}+1\right)}\right)^{\frac{1}{3}}$$

Consequently, the conversion factor K is related to parameter ν and α.

$$\frac{\bar{l}_{cr,shell}}{\bar{l}_{cr,column}}=\frac{\lambda_s^{1/3}\kappa}{\lambda_c^{1/3}\kappa}=\left(\frac{\lambda_s}{\lambda_c}\right)^{\frac{1}{3}}=\frac{1}{K} \tag{2.68}$$

When the graphs are plotted both for the column model and shell model, the dimensionless curing rate of column model should be multiplied by the factor K and the dimensionless critical buckling length of column model should be divided by the factor K.

2.6 Convergence Study

A converence study is necessary for finding and checking the adequate number of polynomial terms, m, k, p and q from Eqs. (2.25) and (2.46), of the approximated displacement functions. As the number increases from 5 to 9, the graph converges as figures below.

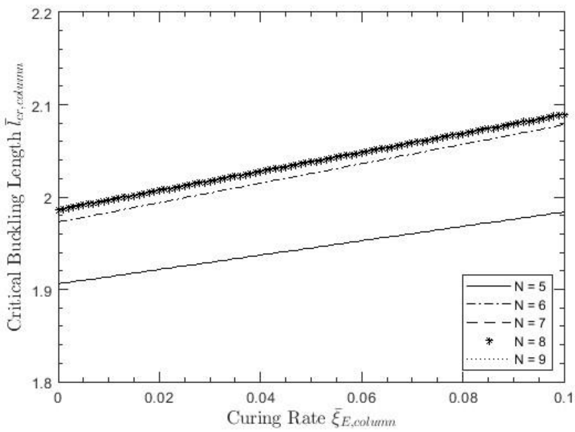

Figure 2-13 Convergence study for the column model : N = 5 ~ 9

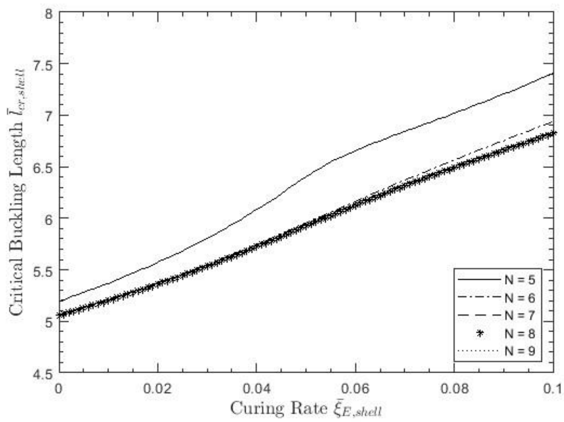

Figure 2-14 Convergence study for the shell model : α = 0.1, $\bar{R}$ = 5.5

If the number of polynomial terms of the displacement functions are more than 7, the value of the dimensionless critical buckling length $\bar{l}_{cr}$ converges rapidly for both of the column model and the shell model. By using the conversion factor K, the column model graphs can be plotted on the shell model coordinate axis.

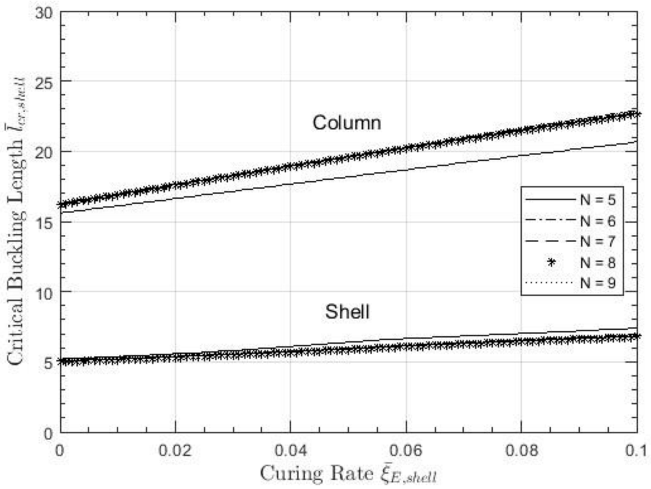

Figure 2-15 Convergence graphs with the column model and the shell model

Selecting the number of polynomial terms as 8 is appropriate to calculate the accurate solution, otherwise the calculation time dramatically increases if the number is greater than 8.

2.7 Plastic Collapse

The 3D printed cylindrical structure may fail by plastic collapse as the compressive stress subjecting to the bottom layer is reaching the yield strength σ_p under its self-weight. The yield criterion for plactic collapse failure can be formulated as

$$\rho g l = \left|\sigma_p\right| = \left|\sigma_c\right| \tag{2.69}$$

where the uniaxial compressive strength of the material σ_c is from the compressive failure criteria described by the maximal stress theory.

Similar to the elastic stiffness expression Eqs. (2.7) and (2.8), the heterogenous yield strength can be expressed as linear function related to the curing rate. The linearly assumed time evolution of the yield strength at the bottom of the cylindrical structure is given by

$$\sigma_{p*}\left(x=0,t\right) = h_*\left(t\right)\sigma_{p,0} \tag{2.70}$$

$$h_*\left(t\right) = 1 + \xi_\sigma t \tag{2.71}$$

where $\sigma_{p,0}$ is an intial yield strength which can be measured from the material at the moment of discharge from the nozzle. Eq. (2.70) can be expressed in terms of the dimensionless Eulerian coordinate in same manner as the elastic stiffness is expressed with the dimensionless Eulerian coordinate $\bar{X} = \frac{\xi_\sigma X}{i}$.

$$\bar{\sigma}_{p*}\left(\bar{X}\right) = \bar{h}_*\left(\bar{X}\right)\sigma_{p,0} \tag{2.72}$$

$$\bar{h}_*\left(\bar{X}\right)=1-\bar{X} \tag{2.73}$$

The location of the bottom layer in terms of the dimensionless coordinate can be written as

$$\delta=\frac{\xi_\sigma l}{\dot{l}} \tag{2.74}$$

Combining Eqs. (2.69), (2.72) and (2.74), the yield condition specializes to

$$\rho g l=\left|\sigma_{p,0}\right|\bar{h}_*\left(\bar{X}\right)\Big|_{\bar{X}=-\delta}=\left|\sigma_{p,0}\right|\left(1+\delta\right)=\left|\sigma_{p,0}\right|\left(1+\frac{\xi_\sigma l}{\dot{l}}\right) \tag{2.75}$$

The length of failure caused by plastic collapse is derived from Eq. (2.75) as

$$l=\frac{\left|\sigma_{p,0}\right|}{\rho g-\frac{\xi_\sigma\left|\sigma_{p,0}\right|}{\dot{l}}} \tag{2.76}$$

The dimensionless plastic collapse length $\bar{l}_p$ and curing rate $\bar{\xi}_\sigma$ are introduced to develop the expression (2.76).

$$\bar{l}_p=\frac{\rho g l_p}{\left|\sigma_{p,0}\right|} \tag{2.77}$$

$$\bar{\xi}_\sigma=\frac{\xi_\sigma\left|\sigma_{p,0}\right|}{\rho g\dot{l}} \tag{2.78}$$

with the range of the dimensionless curing rate $0 \le \bar{\xi}_\sigma < 1$. By setting $l = l_p$ from Eq. (2.76) and substituting the dimensionless parameters in Eq. (2.76), an explicit expression for the dimensionless plastic collapse length can be obtained as follows

$$\bar{l}_p = \frac{1}{1-\bar{\xi}_\sigma} \tag{2.79}$$

Chapter 3. Analysis and Results

3.1 Cylindrical Column Analysis Results

3.1.1 Global buckling length

By using the governing equation of the cylindrical column model, Eq. (2.22), with dimsionless coordinate system and non-dimensional parameters, critical buckling lengths can be predicted for each curing rate. Due to having different components of the paraemet, λ, between column model and shell model, the conversion fator, K, is multiplied to the dimesionless curing rate and the dimensionless length is divided by K. To compare the column curves according to the value of α within the same range of $\bar{\xi}_{E,shell} = 0 \sim 3$, the corresponding values of $\bar{\xi}_{E,column}$ are shown as figure below.

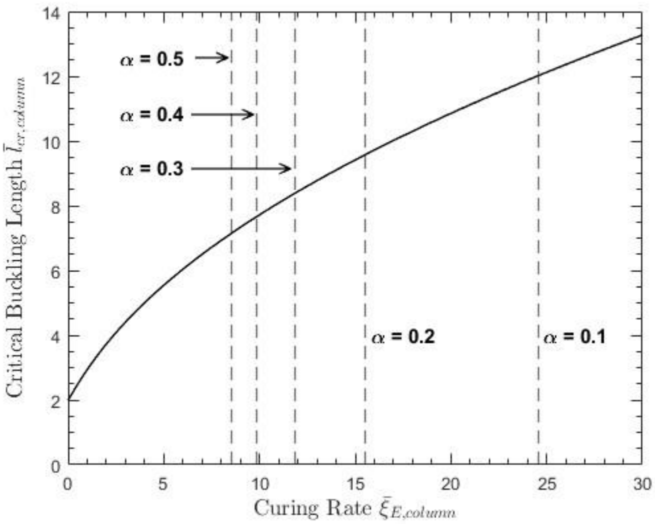

Figure 3-1 Dimensionless criticl buckling length - curing rate curve on the column coordinates system and corresponding value of α

Table 3-1 Values of the conversion factor and α and corresonding values of dimensionless curing rate for column model and shell model

	K	$\bar{\xi}_{E,column}$	$\bar{\xi}_{E,shell}$
$\alpha = 0.5$	0.3506	8.55	3
$\alpha = 0.4$	0.3043	9.85	
$\alpha = 0.3$	0.2526	11.87	
$\alpha = 0.2$	0.1936	15.49	
$\alpha = 0.1$	0.1223	24.54	

After conversion of the parameters from column model to shell model, the dimensionless curing rate decreases and the length increase. Each curve according to the value of α can be plotted as Figure 3-2. If the value of α gets lower, the curve goes upward and the slope becomes steeper.

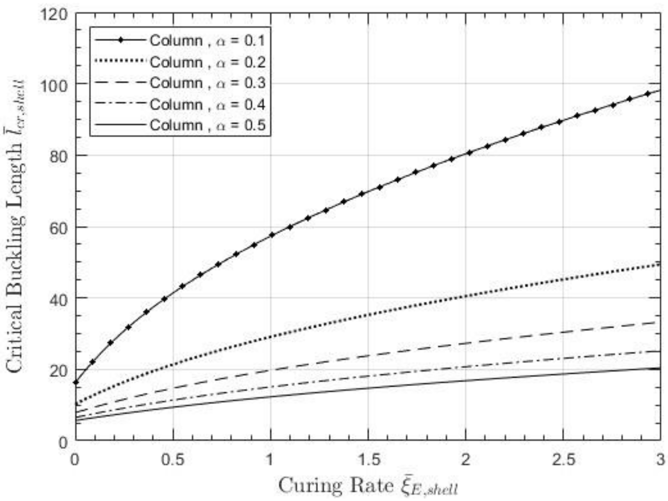

Figure 3-2 Dimensionless criticl buckling length - curing rate curve on the

shell coordinates system according to the value of α

3.1.2 Global buckling mode shape of column model

From Chapter 2, the column model represents the global and the column buckling equation is organized as an eigenvalue problem from the matrix equation for the unknown coefficients. Since the buckling legth is estimated by calculating the non-trivial solution of the matrix equation, determinant of the matrix should be zero. This also means rank of the matrix is smaller than the number of unknwon coefficient and the matrix equation has infinitely many solutions for the unkown coefficients. Thus, to predict the deflection of cylindrical column, a procedure that assumes an unknown coefficient as a specific value is needed, such as C_1 = 1. Then, every unknown coefficient can be calculated by solving the system of linear equations and they are noramlaized by the maximum value. Polynomial equation of the dimensionless lateral deflection is formulated with known coefficients and coordinate $\bar{X}$. Substituting the height $\bar{X}$ from -κ to 0, the deflection $\bar{w}$ is obtained along the height, then the normalized lateral deflection $\bar{w}_{norm}$ can be calculated by dividing $\bar{w}$ by maximum deformation value.

$$\begin{gathered}
\begin{bmatrix} A_{1,1} & \cdots & A_{1,m} \\ \vdots & \ddots & \vdots \\ A_{m,1} & \cdots & A_{m,m} \end{bmatrix} \cdot \begin{bmatrix} C_1 \\ \vdots \\ C_m \end{bmatrix} = \begin{bmatrix} 0 \\ \vdots \\ 0 \end{bmatrix} \\
\det\left|A\right| = 0 \ \ \& \ \ rank\left(A\right) < m \\
\downarrow \\
\begin{bmatrix} A_{1,1} & \cdots & A_{1,m} \\ 0 & \ddots & \vdots \\ 0 & \cdots & 0 \end{bmatrix} \cdot \begin{bmatrix} 1 \\ \vdots \\ C_m \end{bmatrix} = \begin{bmatrix} 0 \\ \vdots \\ 0 \end{bmatrix}
\end{gathered} \tag{3.1}$$

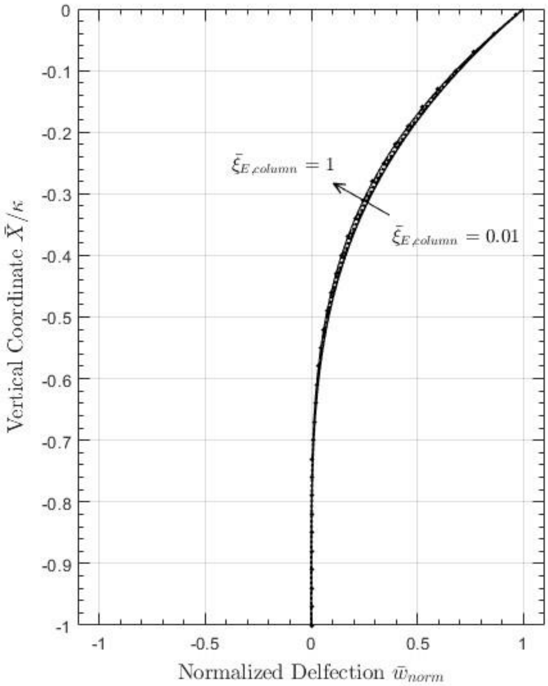

Figure 3-3 Lateral deflection along the height according to the different curing rate from 0.01 to 1

The non-dimensional curing rate is the only parameter affecting to the results of the cylindrical column model. The deflection shape is getting steeper as the curing rate increase, however the differences between the various curing rate are not significant.

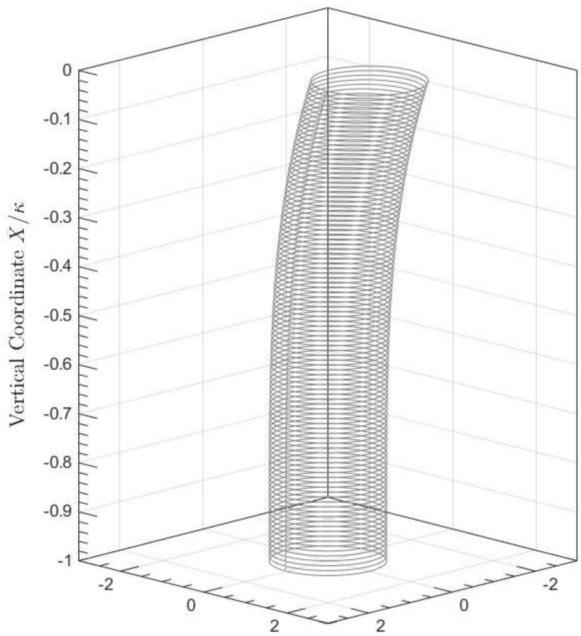

Figure 3-4 Deformed shape of global buckling predicted by column model

According to the lateral deflection $\overline{w}_{norm}$ calculated from above, overall deformed shape of global buckling mode from column model can be predicted and drawn as Figure 3-4. Since the global buckling occurs without any deformation on cross section, the structure buckles only with lateral deflection.

3.2 Cylindrical Shell Ananlysis Results

The parameters used in the cylindrical shell model can be classified into three groups, such as material properties, geometric characteristics and printing variables. All the parameters are arranged in Table 3-2.

Table 3-2 Paramters considered in the cylindrical shell model

Material Properties	**Geometric Characteristics**	**Printing Variables**
ν, ρ, E_0, ξ_E	h, R, α	$\dot{l}$

These parameters affect the performance of the structure in combination since the dimensionless parameters which are used for calculating the diemensionless buckling length consist of them. Thus, to predict the behavior of the shell, identifying the relation between the variables and controlling some parameters to estimate the influence of the other is important process. The results from the numerical analysis will be shown under three control conditions : 1) fixed geometric characteristics α, 2) fixed non-dimensionial radius, and 3) fixed non-dimensionless curing rate.

Table 3-3 Controlled paramters of three analysis conditions

1	**2**	**3**
α	$\bar{R}$	$\bar{\xi}_E$

3.2.1 Fixed geometric characteristics

Controlling α as a specific value represents that the ratio of the layer height to the radius of the structure is constant, which also means when the radius of shell increases, the height of layer increases at a constant ratio. Furthermore, it can be interpreted as a structure, having the same radius and same layer height, is printed by a different material and different printing condition. On the 3-D graphs with the dimensionless radius as x-axis and the dimensionless curing rate as y-axis, the critical buckling length has been predicted when the value of α and n are selected as 0.1 and 1, respectively.

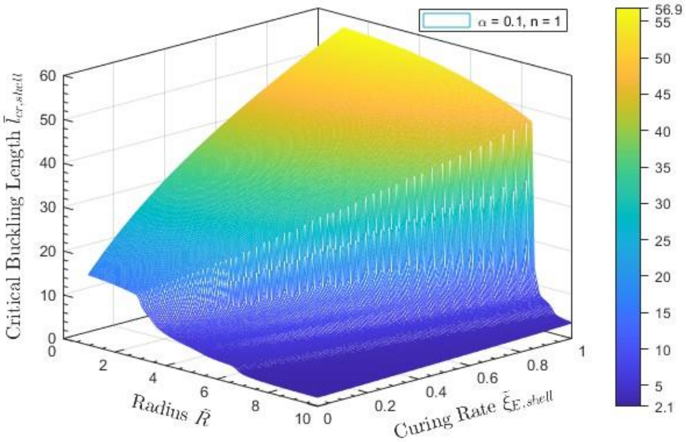

Figure 3-5 $\bar{R}$ - $\bar{\xi}_E$ - $\bar{l}_{cr}$ 3-dimensional graph when α = 0.1 and n = 1

The graph illustrstes that when the non-dimensional radius increases and the non-dimensional curing rate decreases, the non-dimensional buckling length decreases rapidly. The section of the graph at $\bar{R}$ = 1 to 5 are shown below.

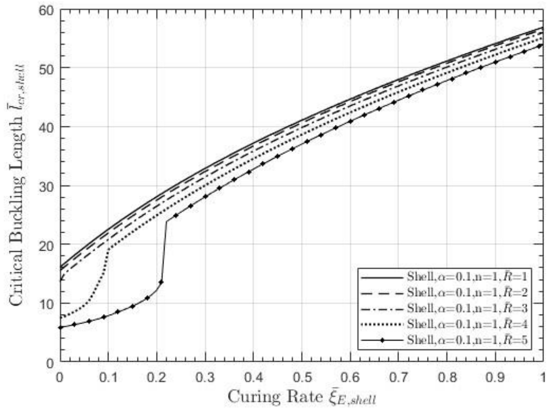

Figure 3-6 Section of the 3-D graph for α = 0.1 and n = 1 conditions at $\bar{R}$ = 1 to 5

From Figure 3-6, the buckling length decreases rapidly between $\bar{R}$ = 3 and 4 at the lower curing rate and the length increases dramatically after 0.06 and 0.21 curing rate for $\bar{R}$ = 4 and 5, respectively. After these points, curves for each $\bar{R}$ increase in a similar form. However, for the large non-dimensional radius, the higher buckling mode is expected and thus the govering buckling length would be lower than mode 1.

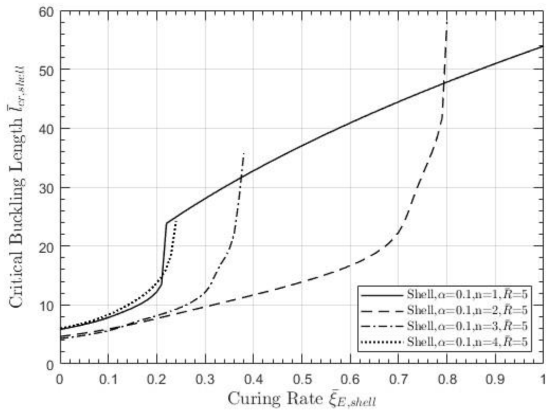

Figure 3-7 Comparion of the buckling length for n = 1 to 4 with same α

Figure 3-7 shows that the expected buckling modes are n = 2 (large curing rate) and 3 (low curing rate) for $\bar{R}$ = 5 and corresponding buckling length is lower than mode n = 1, thus this mode and length governs the buckling. Considering the buckling mode, the shape of graph, Figure 3-5, will be changed and the critical buckling length will decrease for the specific conditions.

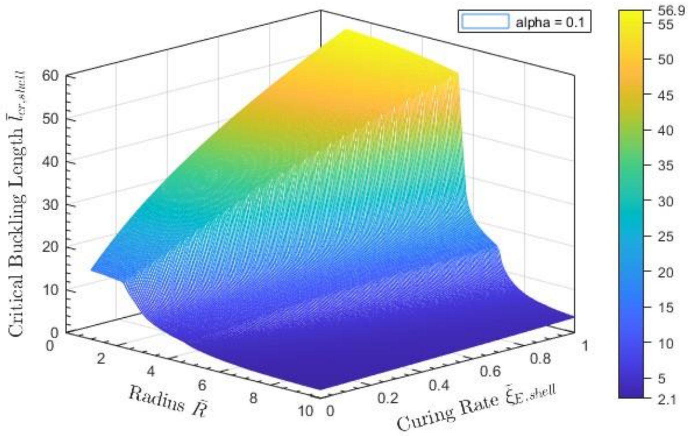

Figure 3-8 Governing $\bar{R}$ - $\bar{\xi}_E$ - $\bar{l}_{cr}$ 3-dimensional graph when α = 0.1

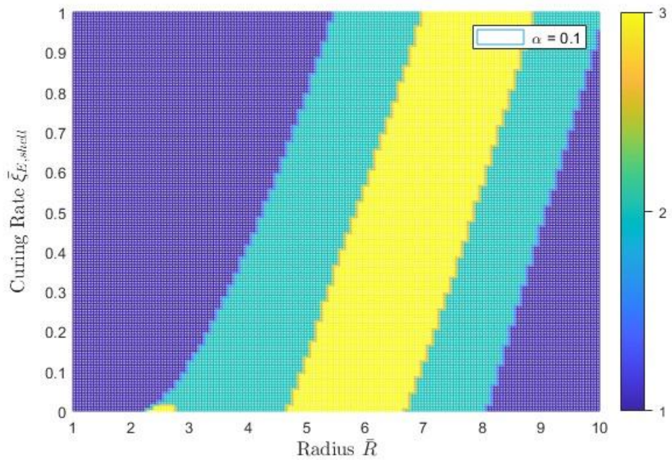

Figure 3-9 Buckling mode when α = 0.1

When the α value of the cylindrical shell is changed, the performance of other cases can be predicted by the graphs below.

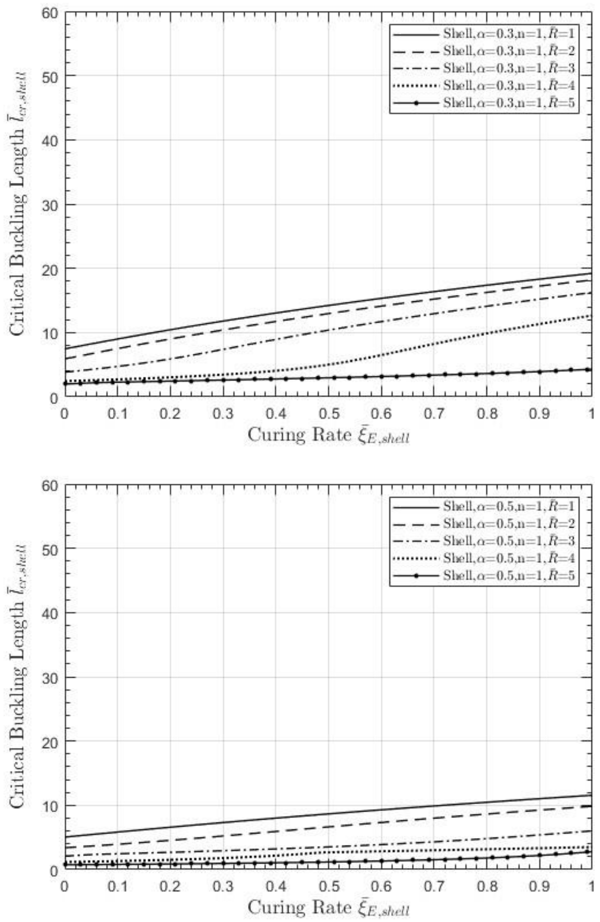

Figure 3-10 Other cases when α = 0.3 and 0.5 with n = 1 and $\bar{R}$ = 1 to 5

If the parameters except for the value of α are constant, as the ratio between the layer height and radius increases, the buckling length decreases, especially rapdily decreasing in the range of α = 0.1 and 0.3.

3.2.2 Fixed non-dimensional radius

The paramter $\bar{R}$ relates to the material properties and α. If the same material is used, in other words, if the material properties using for the anaylsis and the ratio $\frac{R}{h^2}$ are consistent, the $\bar{R}$ value is constant. However, that does not mean α is constant. Thus, depending on whether α is constant or not, the graph can be plotted by 2-dimension or 3-dimension. With considering the buckling mode, a 3-D graph can be plotted when $\bar{R}$ is constant as 5.4865 which is the specific value from the validation experiment for 0.3 m radius sample with the layer height 0.02 m.

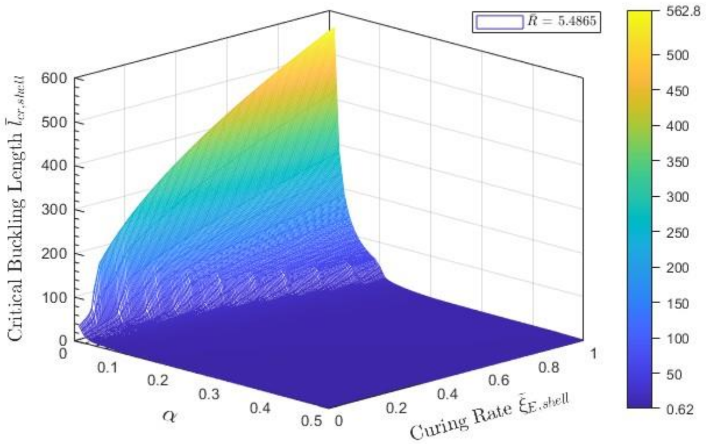

Figure 3-11 Governing α - $\bar{\xi}_E$ - $\bar{l}_{cr}$ 3-dimensional graph when $\bar{R}$ =5.4865

The above figure represents the rapid decreasing of the non-dimensional buckling length at the small α. If the α value and the material properties are already determined during the design process, the $\bar{R}$ value is always same and only 2-D graph obtained by cutting the section of 3-D graph can be used to predict the behavior of the cylindrical shell with considering the buckling mode.

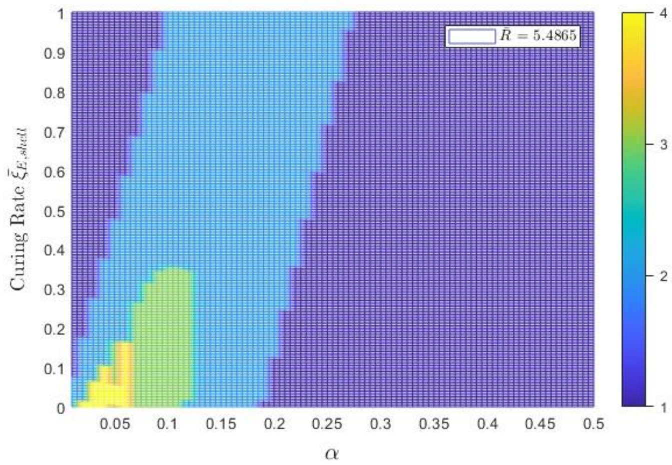

Figure 3-12 Buckling mode when $\bar{R}$ = 5.4865

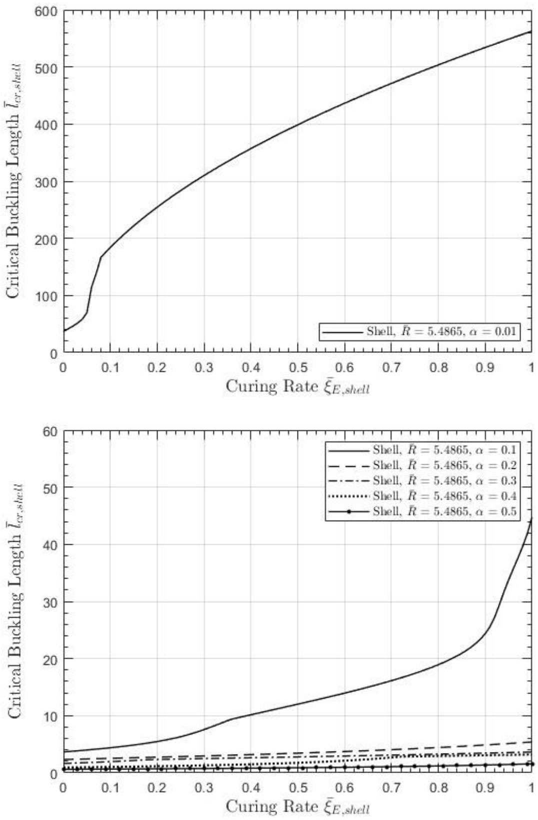

Figure 3-13 2-D graphs cut at (a) α = 0.01, (b) α = 0.1 ~ 0.5

3.2.3 Fixed non-dimensional curing rate

In the real printing process, the raidus of the cylindrical column is commly the major variable, since the material properties are already determined in consideration of the printability and the size of the nozzle is fixed. Furthermore, the growth speed of the length can be determined by the horizontal speed of the nozzle. Then, the non-dimensional curing rate has a constant value. The only variable that affects to the performance of the shell is the radius of the cylindal and α will be determined by the radius.

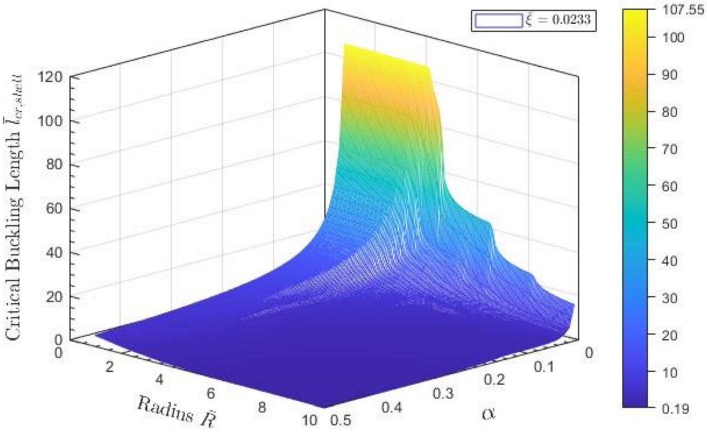

Figure 3-14 Governing $\bar{R}$ - α - $\bar{l}_{cr}$ 3-dimensional graph when $\bar{\xi}_E$= 0.0233

If the target value of the radius of the designed cylindrical structure is decided, the non-dimensional radius $\bar{R}$ and the ratio α can be calculated and then the non-dimensional buckling length is obtained from the one point of the 3-D graph. A value $\bar{\xi}_E$ = 0.0233 is related to the validation experiement which will be dealt from Chapter 5.

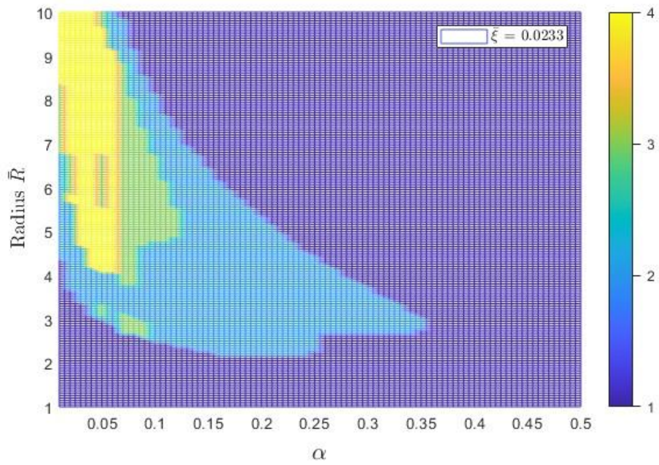

Figure 3-15 Buckling mode when $\bar{\xi}_E$ = 0.0233

3.2.4 Local buckling mode shape of shell model

The cylindrical shell model can show global or local buckling according to the governing buckling mode and it can be compared with the column model. All of the parameters in the shell buckling equation where the determinant of matrix equation is zero should be specified as a value to estimate the lateral deflections. Controlling the parameters according to the three conditions : 1) fixed α and $\bar{\xi}_E$, 2) fixed α and $\bar{R}$ and 3) fixed $\bar{\xi}_E$ and $\bar{R}$.

Conditions	**1**	**2**	**3**
Fixed Parameters	$\alpha,\ \bar{\xi}_E$	$\alpha,\ \bar{R}$	$\bar{\xi}_E,\ \bar{R}$
Variance	$\bar{R}$	$\bar{\xi}_E$	α

First, Figure 3-16 shows the different buckling mode shpes according to the non-dimensionless radius. As the radius increases, the deflection curve has more complex shape in the beginning. Especially when $\bar{R}$ = 3, the cylindrical structure deflects back and forth based on the center of layer, $\bar{w}$ = 0. However, the more radius increases, the structure shows the similar buckling mode shape regardless of the governing buckling mode for each $\bar{R}$.

When the paramters, α and $\bar{R}$, are fixed, for the small curing rates, the structures collapse in almost the same mode shape. However, as the curing rate increases, the structure shows complex deflection curve.

There is less tendency when the parameter α increases while the other parameters are fixed. Althought the deflection curves seem to converge until α increases from 0.01 to 0.4, when α is 0.5, the structure deflects into complex shape.

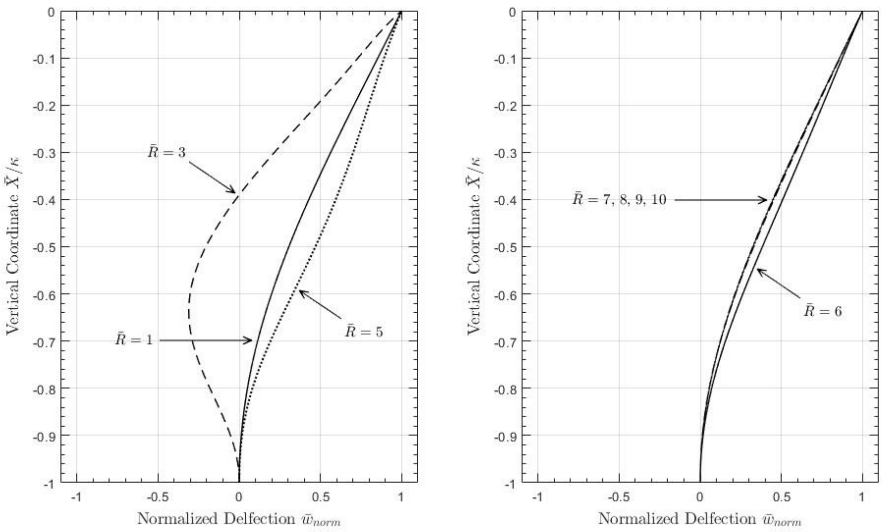

Figure 3-16 Lateral deflections according the different $\bar{R}$ and fixed paramters, α = 0.1 and $\bar{\xi}_E$ = 0.1

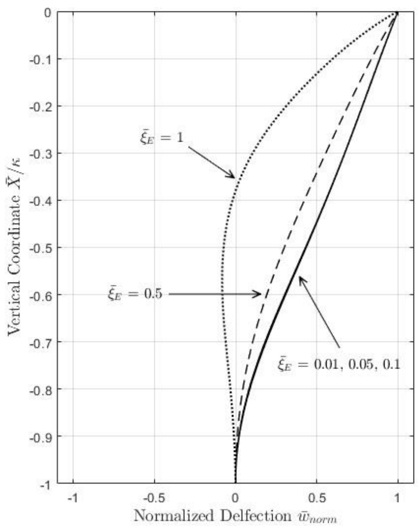

Figure 3-17 Lateral deflections according the different $\bar{\xi}_E$ and fixed paramters, α = 0.1 and $\bar{R}$ = 5.4865

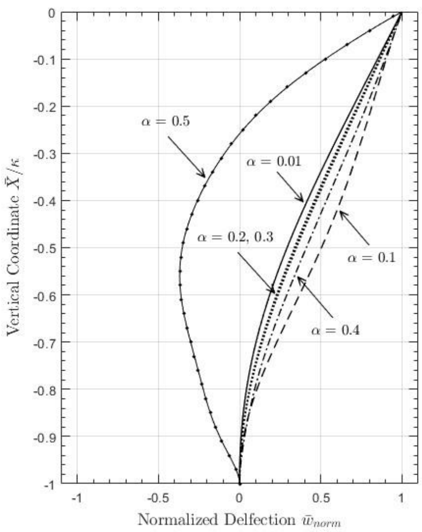

Figure 3-18 Lateral deflections according the different α and fixed paramters, $\bar{\xi}_E$ = 0.0233 and $\bar{R}$ = 5

Compared to the column model, to predict the deformed shape of local buckling from shell model, the sinual terms are also included as Eq. (2.45). Cosine term is multiplied to the radial displacement $\bar{w}$ and sine term is multiplied to the circumferential displacement $\bar{v}$. Since these terms are multiplied, the cross section of shell structure is deformed differently along the height according to the calculated displacement like above. Overall deformed shapes of shell structures with different governing buckling modes are shown as following figures.

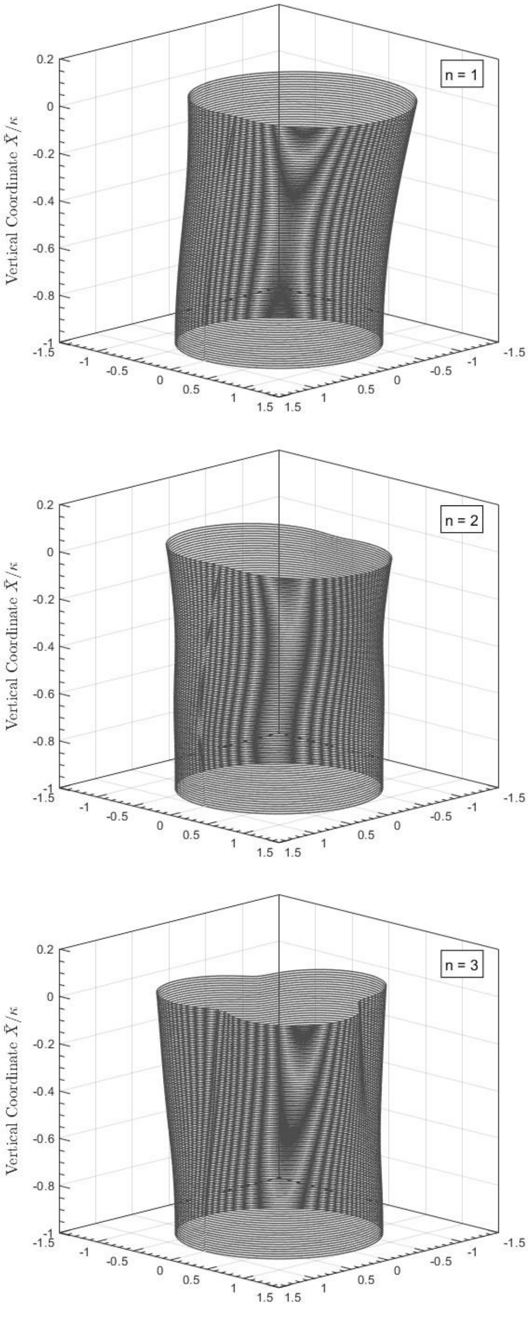

Figure 3-19 Deformed shape of local buckling predicted by shell model with different buckling mode n

3.2.5 Shell structure with geometric imperfection

Additionally, as a final step, the effect of geometric imperfections on the shell buckling behavior is explored by decomposing the dimensionless deflection $\bar{w}$ along the height as

$$\bar{w}\left(\bar{X}\right) = \bar{w}^0 + \bar{w}^F \tag{3.2}$$

where $\bar{w}^0$ is the geometric imperfections and $\bar{w}^F$ is the deflection under the applied load, in this case self-weight of upper layers, and computing the buckling response. The imperfection profile in terms of Lagrangian coordinate x can be idealised with the combination of harmonic and exponential terms as

$$w^0 = w^0\left(x\right) = w_m^0\left(-\sin\left(\frac{2\pi}{n_t t_l}x\right) + \frac{2\pi}{\omega n_t t_l}\left[1-\exp\left(-\omega x\right)\right]\right) \tag{3.3}$$

where w_m^0 is the amplitude of the imperfection, n_t is the number of printed layers defining the wavelength of the imperfection profile, t_l is the height of a printed layer and ω is a factor quantifying the influence length of the exponential term at the boundary $x = 0$. This admissible equation can be transformed in terms of the dimensionless Eulerian coordinate $\bar{X}$ as

$$\bar{w}^0\left(\bar{X}\right) = \bar{w}_m^0\left(-\sin\left(\bar{k}_w\left(\bar{X}+\kappa\right)\right) + \bar{\tau}\left[1-\exp\left(-\frac{\bar{k}_w}{\bar{\tau}}\left(\bar{X}+\kappa\right)\right)\right]\right) \tag{3.4}$$

with the dimensionless imperfection amplitude, $\bar{w}_m^0 = \frac{w_m^0}{h}$, the dimensionless wavenumber $\bar{k}_w = \frac{2\pi \dot{l}}{n_t t_l \xi_E}$ and the boundary factor $\bar{\tau} = \frac{2\pi}{\omega n_t t_l}$.

When applying the decamped dimensionless displacement $\bar{w}$ to Eq. (2.63), the initial imperfections are assumed that they do not generate stresses, in other words, the strain energy under the initial imperfections is zero. In accordance with this assumption, linear equations obtained from the partial differential for unknown coefficients turn into the following non-homogeneous form.

$$\begin{bmatrix} A_{1,1} & \cdots & A_{1,m} \\ \vdots & \ddots & \vdots \\ A_{m,1} & \cdots & A_{m,m} \end{bmatrix} \cdot \begin{bmatrix} C_1 \\ \vdots \\ C_m \end{bmatrix} = \begin{bmatrix} B_1 \\ \vdots \\ B_m \end{bmatrix} \tag{3.5}$$

Since Eq. (3.5) consists of five non-dimensional parameters and has non-homogeneous form, calculating the critical buckling length directly is not possible. However, the unknown coefficients of displacements can be predicted under specific conditions, in other words, under fixed values of parameters. The deflection $\bar{w}$ at the top $\bar{X}$ = 0 of cylindrical structure during 3D printing can be estimated as the length of structure increases.

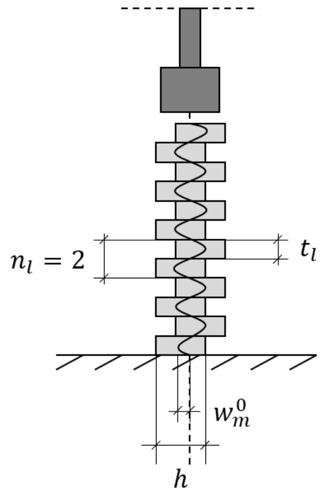

Figure 3-20 Shell structure with geometric imperfection during 3D printing

The influence of exponential term in Eq. (3.4) is assumed relatively small by taking the boundary factor $\bar{\tau}$ = 0.5. Thus, the imperfection is determined by the two paramters, $\bar{w}_m^0$ and $\bar{k}_w$. Figure 3-21 and 3-22 illustrates the deflection at the top of cylindrical structure for two different imperfection amplitude $\bar{w}_m^0$ = 0.01 and 0.05 and six different wavenumber $\bar{k}_w$ = 0, 1, 5, 20, 60 and 120.

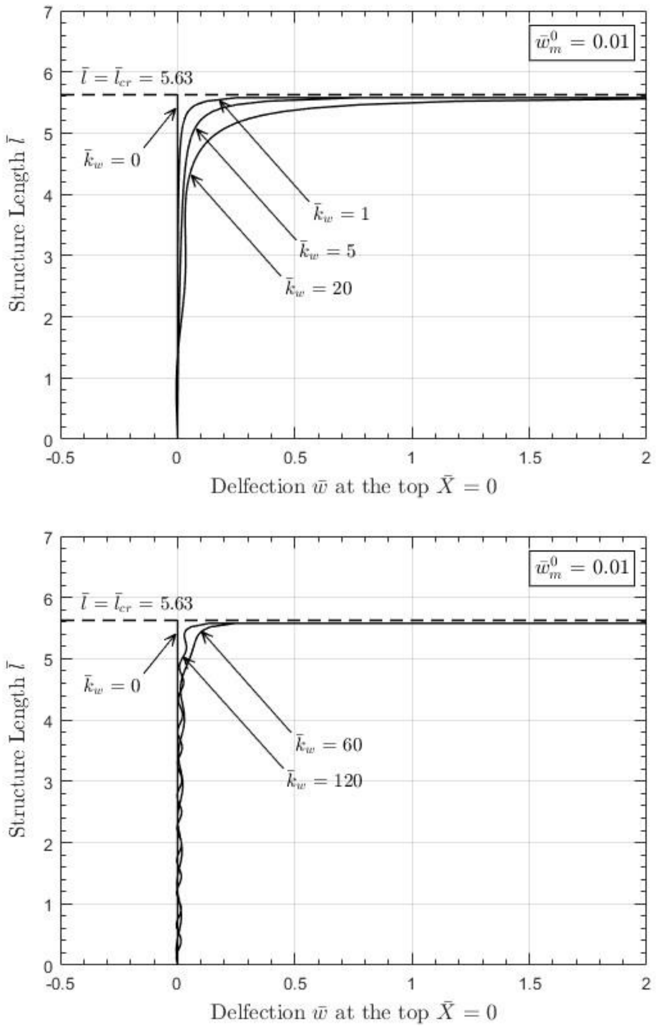

Figure 3-21 Deflection $\bar{w}$ at the top $\bar{X}$ = 0 of structure for $\bar{w}_m^0$ = 0.01

A horizontal dashed line indicates the critical buckling length calculated from buckling equation under certain condition, α = 0.1, n = 3, $\bar{\xi}$ = 0.1 and $\bar{R}$ = 5, which does not consider geometric imperfection. A vertically straight line when the wavenumber is zero represents the bifurcation buckling path when the structure is gemetrically perfectly printed. As wavenumber $\bar{k}_w$ increases, the deflection at the top increases in the beginning, and then decreases. Furthermore, the deflection curve has more sinusoidal wave and complex profile as wavenumber increases, and it is close to the bifurcation buckling path.

From Figure 3-21 and 3-22, both for the small and large imperfection amplitudes, the curves for the different wavenumber asymptote towards the crical buckling length. However, for the large imperfection amplitude $\bar{w}_m^0$ = 0.05, the converegence occurs with the larger deflection than small amplitude.

In conclusion, when the geometric imperfection generated on the cylindrical structure during 3D printing has a relatively small amplitude and large wavenumber, the bifurcation buckling length calculated from homogeneous buckling equation serves as an adequate design value.

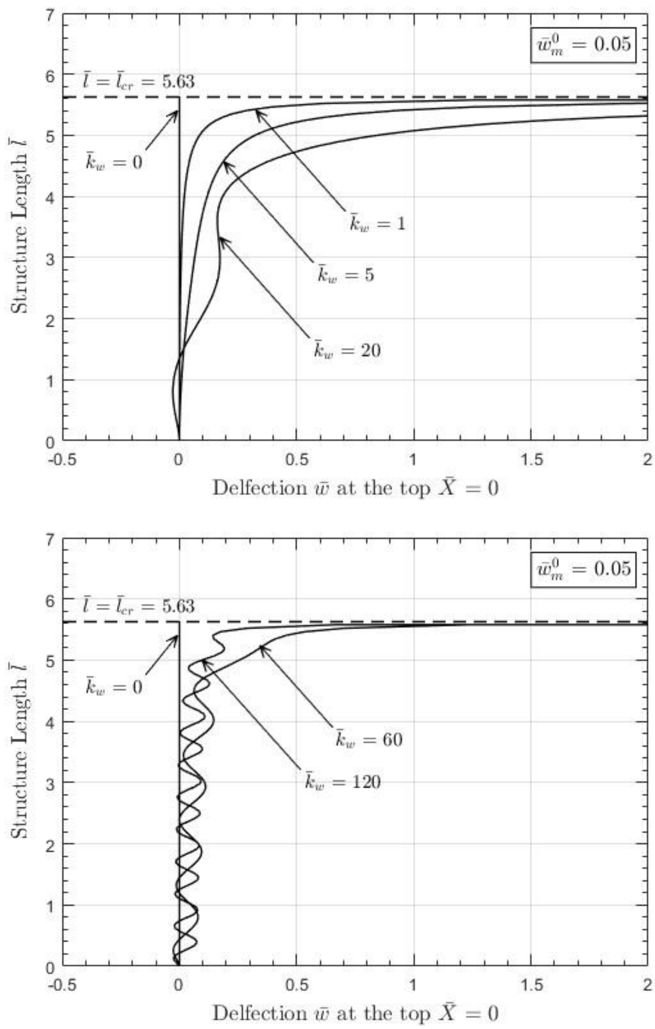

Figure 3-22 Deflection $\bar{w}$ at the top $\bar{X}$ = 0 of structure for $\bar{w}_m^0$ = 0.05

3.3 Comparison between Cylindrical Column and Shell

The analysis for the cylindrical column depends on the value of α regardless of $\bar{R}$ when it converts to the shell model coordinate from its own coordinate. Thus, to compare the two differnet models, three types of the 3-D graphs from each condition can be used. First, when α is constant, as shown in Figure 3-23, the buckling length of the column model is always higher than shell model with $\bar{R}$ = 1 ~ 10 and $\bar{\xi}_E$ = 0 ~ 1.

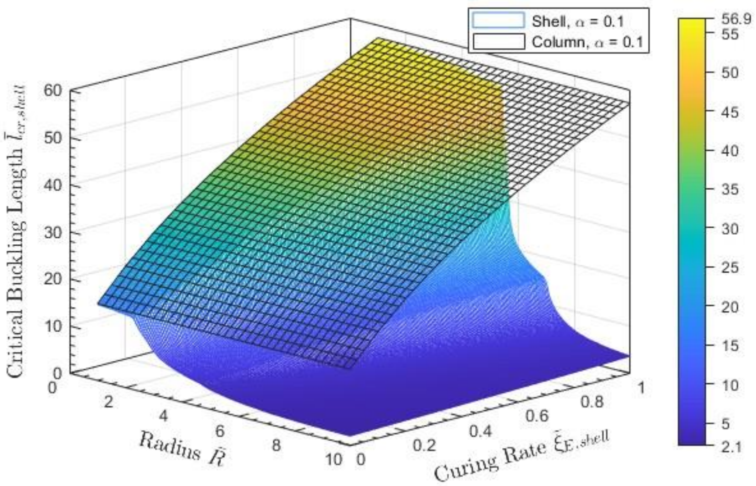

Figure 3-23 Governing $\bar{R}$ - $\bar{\xi}_E$ - $\bar{l}_{cr}$ 3-D graph for column and shell model when α = 0.1

For the shell having small non-dimensional radius and high curing rate, the analysis results from column and shell is almost same. Figure 3-24 shows the section of the 3-D graph at $\bar{R}$ = 1 to 5 and it seems column and shell curves converge as the curing rate is higher.

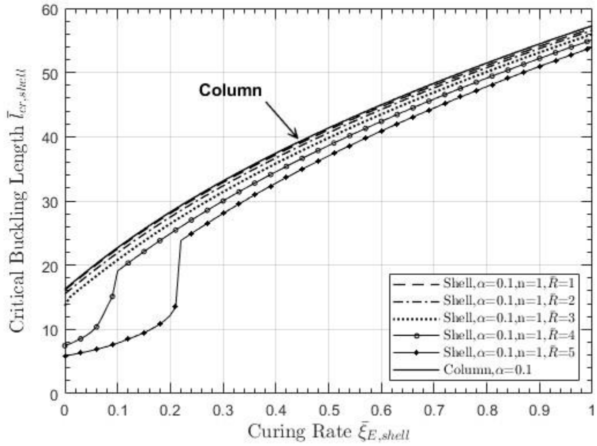

Figure 3-24 Comparison between column and shell model with α = 0.1 and n = 1 conditions for $\bar{R}$ = 1 to 5

Following figures represent the analysis results both for column and shell model with the conditions of the constant $\bar{R}$ and $\bar{\xi}_E$, respectively.

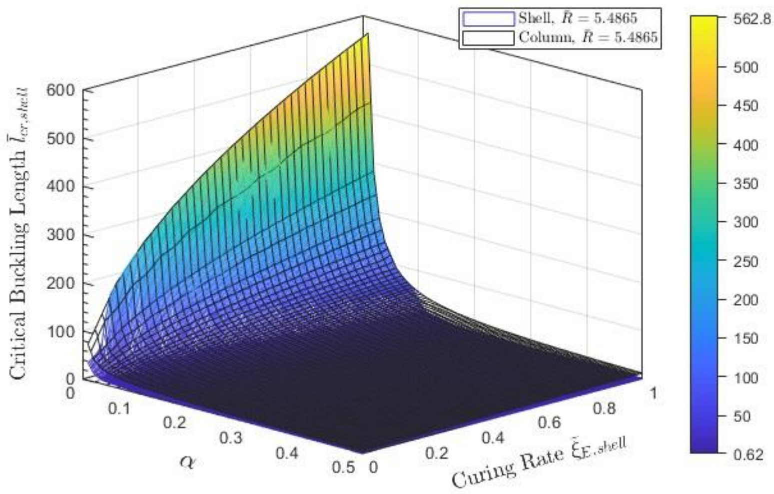

Figure 3-25 Governing α - $\bar{\xi}_E$ - $\bar{l}_{cr}$ 3-D graph for column and shell model when $\bar{R}$ = 5.4865

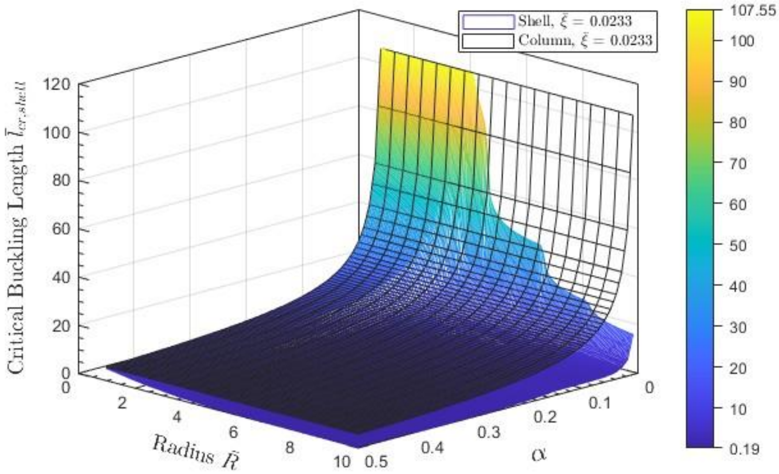

Figure 3-26 Governing $\bar{R}$ - α - $\bar{l}_{cr}$ 3-D graph for column and shell model when $\bar{\xi}_E$ = 0.0233

Comparing the anaylsis results from the column model with the shell model, three figures which have different condition represent that the non-dimensional buckling length from the column model is always higher than from the shell model. However, as the values of the parameters, $\bar{R}$, $\bar{\xi}_E$ and α get smaller, the differences between the two models get smaller.

3.4 Plastic Collpase Analysis Results

The non-dimensional plastic collapse length can be calculated from the simple equation. Since the non-dimensionless curing rate for the compressive strength ranges 0 or more and less than 1, the non-dimensionless plastic collapse length is 1 at zero curing rate and increases infinitely when the curing rate gets closer to 1. A conversion from the plastic collapse coordinate to the shell model coordinate is not possible, since the parameters used in the dimensionless parameter are not same.

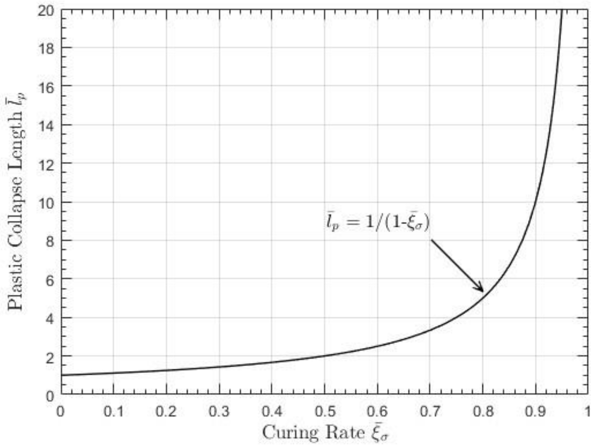

Figure 3-27 Plastic collapse length from zero curing rate and under one

3.5 Case Study for Three Models

Understanding the meaning of the non-dimensional values is difficult and complicated, since various parameters which indicates the properties of material or geometric and printing conditions exist. Thus, to show clearly how to predict the performance of the cylindrical structures by using the suggested models, the case study has been conducted to predict the governing failure length which can be estimated by comparing the results from the column, shell and plastic collapse models. The properties of the material which will be handled at Chapter 4, the geometric configuration and printing conditions are chosen as below.

Table 3-4 Concrete mixture proportions

Material Properties		**Geometric Characteristics**		**Printing Variables**	
ν	0.3	h	20 mm	v_n	0.1 m/sec
ρ	1850 kg/m^3				
E_0	35.02 kPa	d	10 mm		
ξ_E	0. 35 Pa/sec				

The analysis is predicting the failure length from each model according to the various radius, from 40mm to 400mm. The buckling length is plotted as a line, the column as a dot line and dash-dot line for the yield failure. Gray dash lines represent the changing points of the govering failure mode.

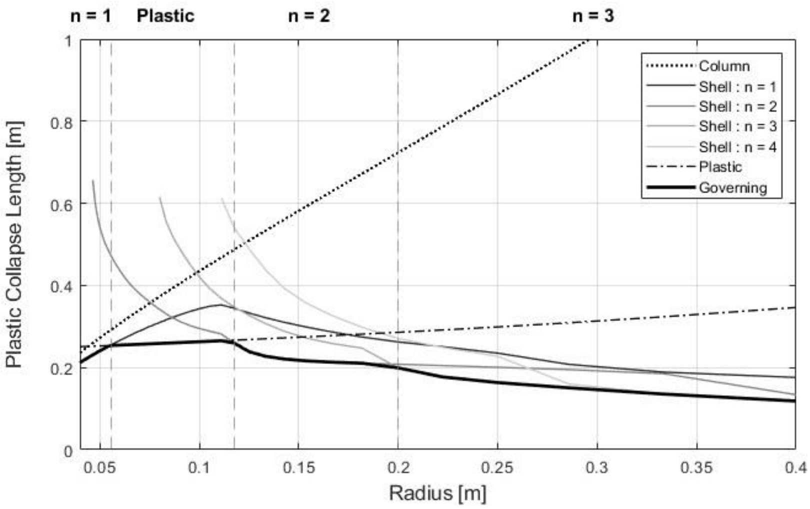

Figure 3-28 Case study with the column, shell and plastic models and governing failure length and mode

As shown in the figure above, the cylindrical structure having large radius buckles earlier and has higher buckling mode. However, for smaller structure, it collpases at higher and by the material yielding at the bottom layer. Furthermore, the column model overestimates the buckling length for the cylindrical structures.

Chapter 4. Material Tests and Properties

4.1 Concrete Mixture Proportions

The printabiliy of the material used in 3D printing is relate to the rheological properties of the fresh concrete, such as yield stress and plastic viscosity. A material mixture design for validation experiments targets to low plastic viscosity to easily slip inside the hose, high initial yield stress to sustain shape of layer and prevent segregation. The usage of cement and flyash is same and four types of sand are used for half of cement. The ratio of water to cement is 0.64 which is high relative to the normal concretes and superplasticizer is used as much as 0.375% of cement. Table 4-1 shows the overall proportions of the concrete material which is used for the experiments.

Table 4-1 Concret mixture proportions

OPC	FA	SF	W	Sand	PP	SP
1	1	0.1	0.64	0.5	0.0015	0.00375

Table 4-2 Particle sizes and proportions of four types of sand

	Size [mm]	Proportion
Sand5	0.6 ~ 1.2	0.25
Sand6	0.25 ~ 0.6	0.25
Sand7	0.15 ~ 0.25	0.1
Sand8	~ 0.15	0.4

4.2 Fresh Concrete Properties

4.2.1 Modulus of elasticity

From Chapter 2.2.2, the curing function of the concrete material is assumed as linear function. Uniaxial unconfined compression tests for estimating the stiffness modulus of fresh concrete are conducted by using universal testing machine. The experiments are conducted from 15 minutes to 70 minutes in 15 minutes intervals and five samples are tested in each time. Here, '15 minutes' refers to the time elapsed since the concrete begins to be mixed. The samples are cylinder diameter of 50mm and 100mm height. The displacement-controlled tests are performed at a rate of 20mm/min and the average test time is 2 min which is equal to 40% strain [9].

Figure 4-1 Samples for universal testing machine

Laod - displacement graphs of the experiements show that the load initially increases approximately linearly and keeps increasing as the verical displacement increases. The average load increases for older concrete as Figure 4-1.

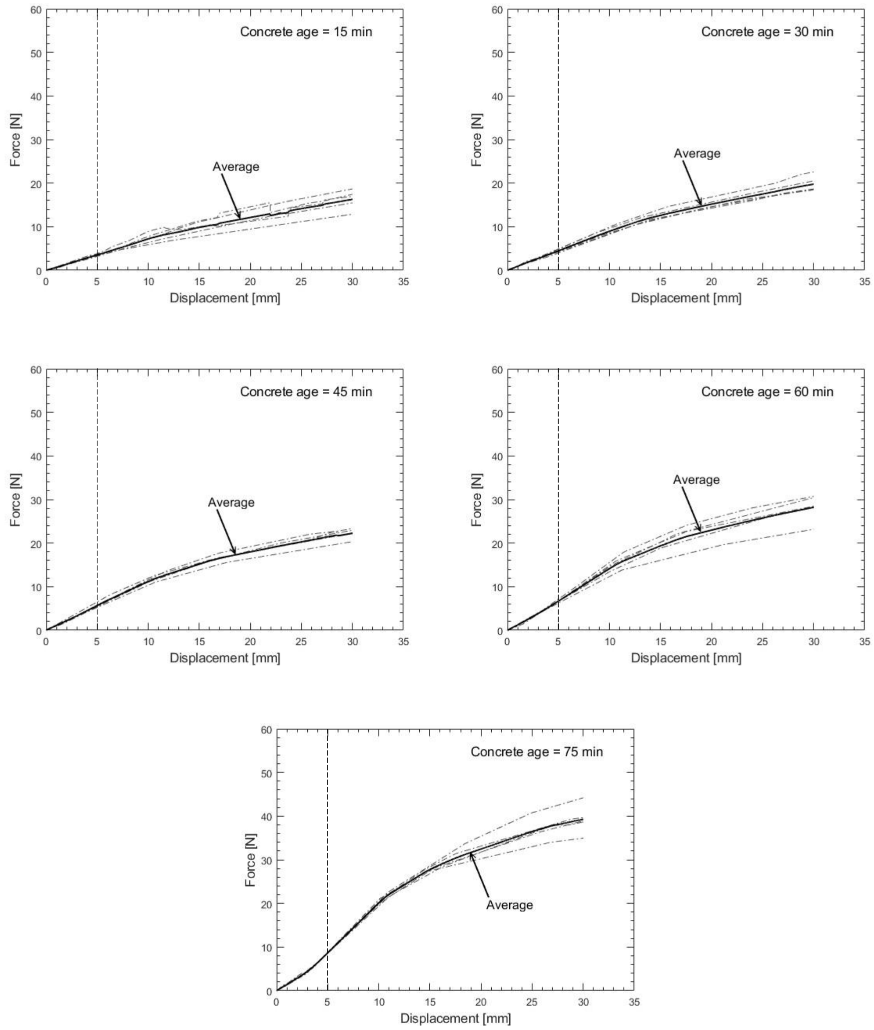

Figure 4-2 Force - displacement graphs of compression tests for concrete age 15 to 75 minutes

Young's modulus of each specimens can be measured at 5% strain since in this range the slopes of the graphs are almost linear for each concrete age. The values of stiffness modulus from each sample are shown in Table 4-3.

Table 4-3 Values of modulus of elasticiy from each samples and concrete age

	15 min [kPa]	**30 min [kPa]**	**45 min [kPa]**	**60 min [kPa]**	**75 min [kPa]**
Sample 1	40.31	45.41	53.27	65.32	80.58
Sample 2	32.18	40.63	66.35	63.83	80.80
Sample 3	33.92	48.18	53.13	70.25	78.66
Sample 4	37.43	44.46	55.72	64.69	83.17
Sample 5	35.19	49.87	56.68	67.22	80.59
Average	35.81	45.71	57.03	66.26	80.76

A linear function for modulus of elasticity can be obtained from the linear regression on the average values from each concrete age. The stifness modulus of the fresh concrete is initaially 23.98 kPa and linearly increases by the rate of 0.7364 kPa/min.

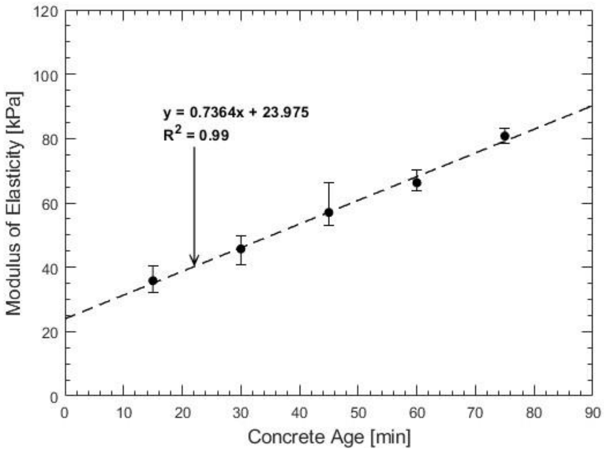

Figure 4-3 Measured modulus of elasticity and linear regression function

4.2.2 Compressive strength

A compressive strength of the material can be measured with the tests dealt from the previous chapter. However, to calculate the stresses of each sample, updated cross - sectional area are necessary, since the large lateral deformations occur. The horizontal strain is measrued using edge detection technique by MATLAB program. The boundary of the sample in the video is tracked by green line having coordinate values which indicate the location. Then, the average horizontal distance between two side lines can be calculated. Comparing the average distance from previous image and current image, the average horizontal strain between two images is obtained. Since original diameter of cylinder is already given as 50mm, the updated diameter can be measured by multiplying the strain stey by step.

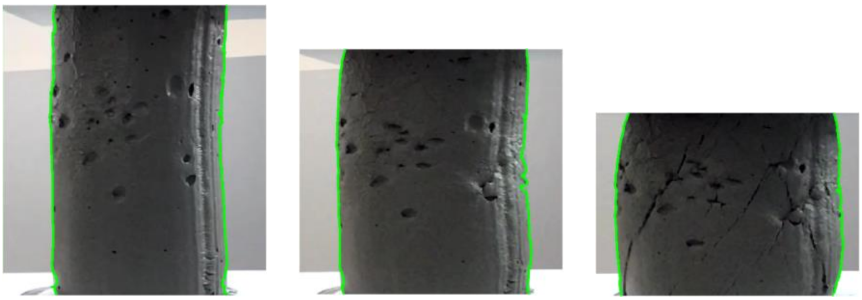

Figure 4-4 Tracking the boundary of sample using edge detection technique

Dividing the increased cross-sectional area of cylinder due to the lateral deformation, the compressive stress can be calculated diving the force by updated area. Then, as shown in Figure 4-5, the slope of stress - strain curve is gradually decreasing and the peak occur, especially for older samples.

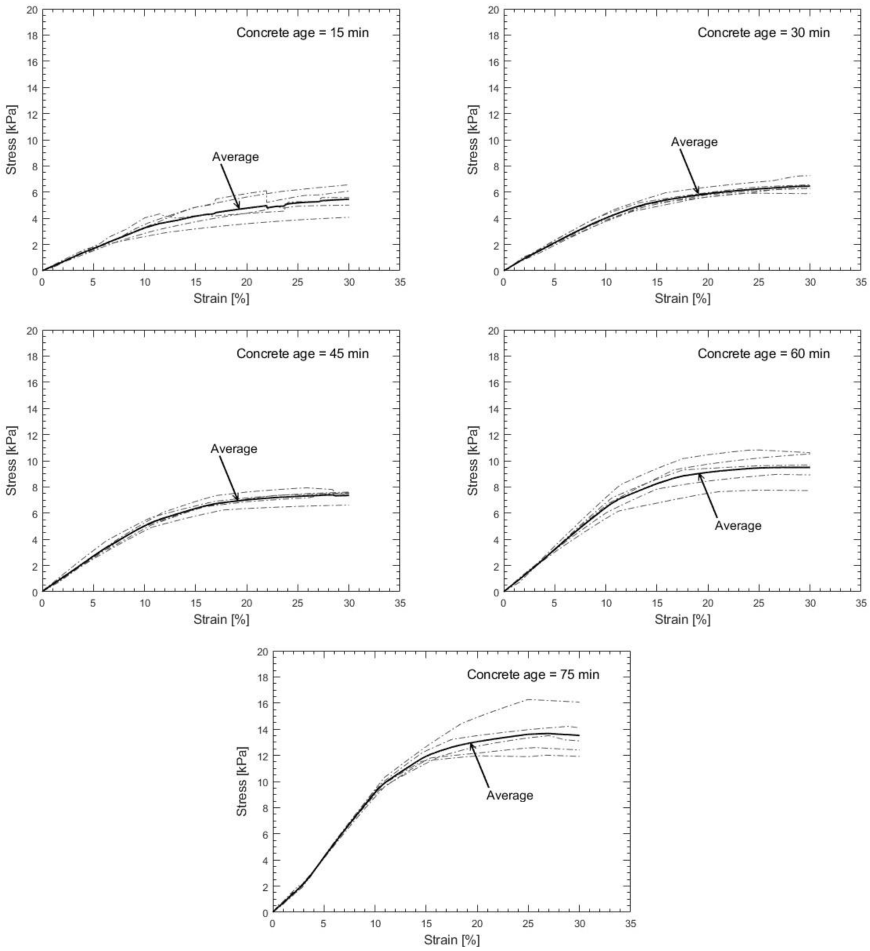

Figure 4-5 Stress - strain curves of compression tests for concrete age 15 to 75

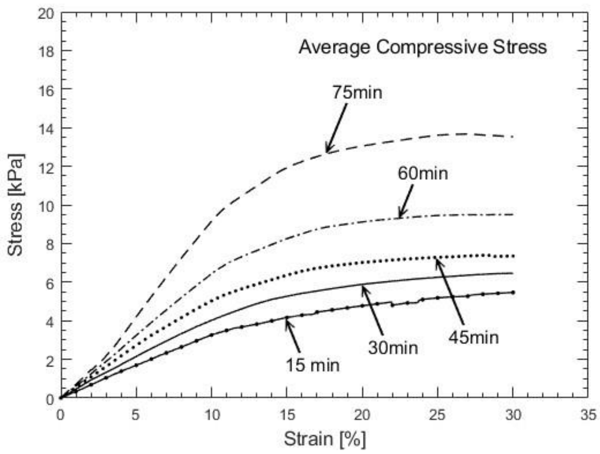

Figure 4-6 Average compressive stresses for concrete age 15 to 75

However, since the cracks or failure occur as the lateral deformation increases, the data should be cut-off at the moment when the cracks occur. These points are different according to the samples. Table 4-4 shows the cut-off strain where the cracks occur.

Table 4-4 Vertical strain when the failure occrus

	15 min [%]	**30 min [%]**	**45 min [%]**	**60 min [%]**	**75 min [%]**
Sample 1	31	29	34	29	25
Sample 2	24	28	30	30	31
Sample 3	34	23	34	25	30
Sample 4	27	30	30	26	23
Sample 5	25	28	28	30	33

The stresses corresponding to the vertical strain from Table 4-4 are arranged as following table. However, the outliers exist in each concrete age.

Table 4-5 Stresses corresponding to the strain obtained from Table 4-4

	15 min [kPa]	30 min [kPa]	45 min [kPa]	60 min [kPa]	75 min [kPa]
Sample 1	4.11	5.89	<u>6.63</u>	9.68	11.90
Sample 2	4.83	6.26	7.61	<u>7.76</u>	13.05
Sample 3	<u>6.75</u>	6.24	7.66	10.82	<u>16.07</u>
Sample 4	5.28	6.17	7.50	10.53	13.79
Sample 5	5.67	<u>7.12</u>	7.82	8.93	12.36
Average	5.33	6.34	7.44	9.54	13.44
Modified	4.97	6.14	7.65	9.99	12.78

By eliminating the outliers expressed as underline in Table 4-5, the average compressive stress increases or decreases. The data fits better with the linear function, thus assuming the curing function for compressive strength as linear is appropriate method. An initial compressive strength can be estimated as 2.46 kPa and the curing rate for the compressive strength is 0.13 kPa/min.

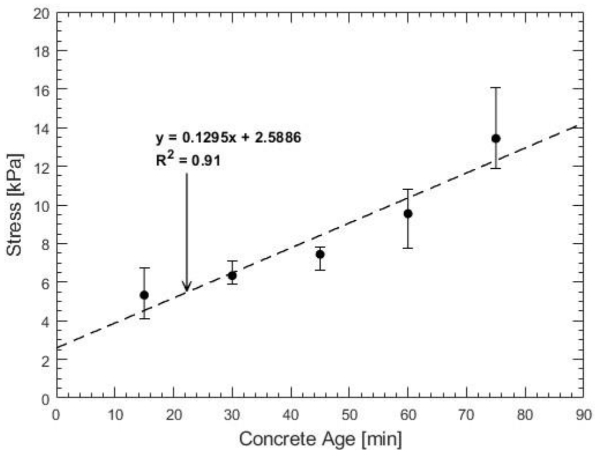

Figure 4-7 Growth of compressive strength with total data

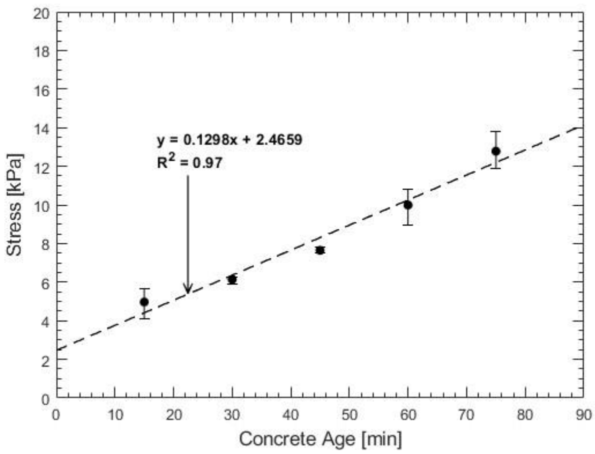

Figure 4-8 Growth of compressive strength without outliers

4.2.3 Plastic viscosity

The plastic viscosity is measured by Viskomat rheometer machine. Three liter of the fresh material is needed for one sample. Totally, 9 samples are tested and each sample is used up to 7 times with interval of 5 minutes. A fishbone probe rotates at a linearly incrasing speed from 0 rpm to 80 rpm in 1.67 minutes or 2.67 minutes to prevent the slippage between the material and bowl. From the obtained data, the data is cut-off at the point where the R square is greater than 0.9, then the value of slope which has N-mm/rpm dimension can be obtained by linear regression.

Figure 4-9 Viskomat rheometer machine and testing image

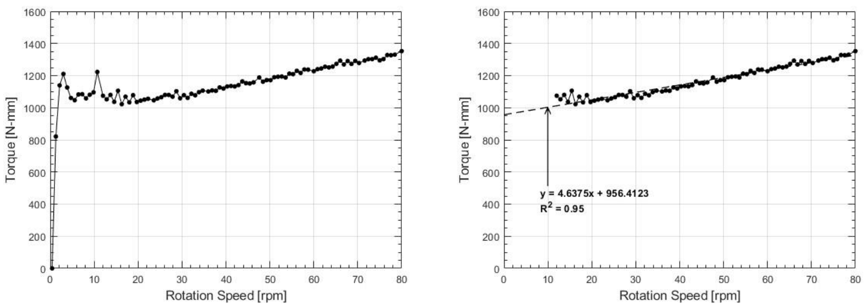

Figure 4-10 Growth of compressive strength without outliers

Sine the dimesion of slope estimated from the data as show in Figure 4-10 is N-mm/rpm, a calibration constant, 2.62 which is from the manul of Viskomat machine, shoule be multiplied to the slope to get a dimension Pa-sec. Total 60 data is plotted on the graph according to the time and Figure 4-11 shows that the average plastic viscosity from different concrete age is almost similar regardless of time effect. Thus, the plastic viscosity of the material used can be assumed as approximately constant as 11.53 Pa-sec.

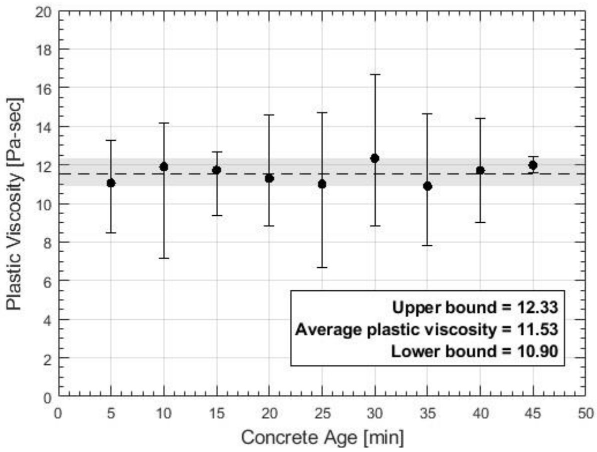

Figure 4-11 Plastic viscosity with lower and upper bound

4.2.4 Yield stress

By using same rheometer machine but with different type of probe, vane probe, the yield stress can be measured as Figure 4-12. The bowl where the material is in rotates every 10 minutes at 0.33 rpm during 10 seconds. The peak torque occurs during rotation as shown in Figure 4-12. As in the previous chapter, a calibration constant, 1.45343, will be multiplied to the peak value to convert the dimension from torque [N-mm] to stress [N/m^2] and this value represents the yield stress of matieral at that curing time.

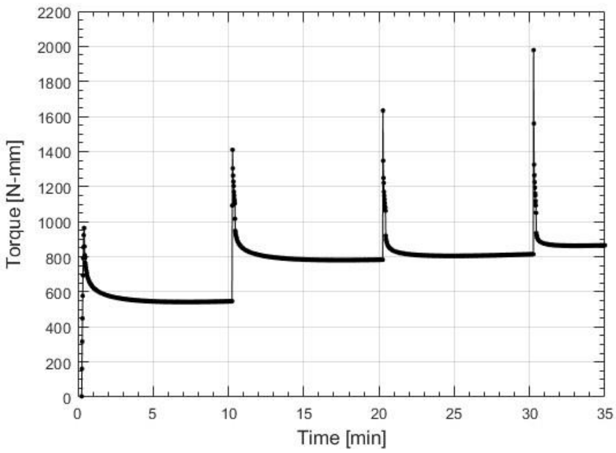

Figure 4-12 Data of a sample with linearly increasing peak value

Using the average yield stress at each curing time and doing linear regression, data fits well in linear function as Figure 4-13 and assuming the evolution of the yield stress linear with the time is proved from the articles written by Roussel.

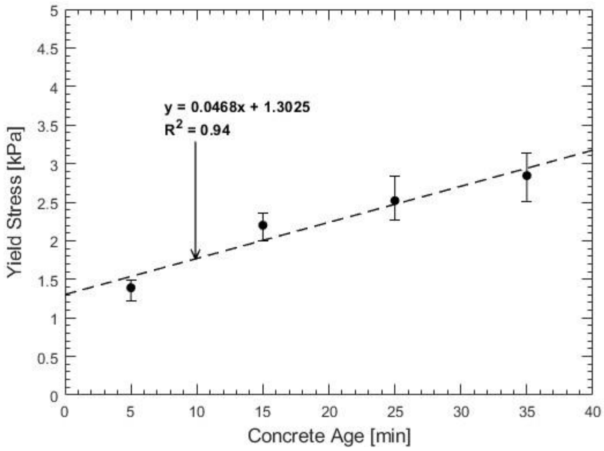

Figure 4-13 Growth of yield stress with linear regression function

4.2.5 Bond Strength

To sufficiently initiate the flow in the printed layer at rest to mix adjacent layers, the stresses generated by the flow of the upper layer should be greater than the staic yield stress of the resting layer. The stresses generated between two layers can be approximately decomposed into independent normal stresses and shear stresses. The normal stresses generated by the printing layer are related to the weight of the layer as below [10]

$$\begin{aligned} \sigma_{xx} = \sigma_{yy} &= \frac{\rho g d}{6} \\ \sigma_{zz} &= -\frac{\rho g d}{3} \end{aligned} \tag{4.1}$$

with the density of the material ρ, the acceleration of gravity g and the depth of the printing layer d.

The shear stress generated at the interface between the adjacent layers by the printing of the upper layer can be expressed as follows

$$\tau_{xz} = \tau_{00} + \mu_p \frac{2V}{d} \tag{4.2}$$

where τ_{00} is the initial static yield stress of the material, μ_p represents the plastic viscosity and the horizontall print speed of the concrete V divided by the average depth $\frac{d}{2}$ of the second layer equals the shear rate.

Considering a Von Mises criterion as the plasticity criterion, a resting time, which represents a maximum printing period to mix the adjacent layers, can be formulated by expressing the stress generated by the upper layer equals the yield stress of the lower layer.

$$\frac{\sigma_{xx}{}^{2}+\sigma_{yy}{}^{2}+\sigma_{zz}{}^{2}}{2}+\tau_{xz}{}^{2}\geq\tau_{0}{}^{2}\left(t_{rest}\right) \tag{4.3}$$

whereby $\tau_0(t_{rest})$ representing the static yield stress of the printed layer after the resting time t_{rest} is given by

$$\tau_0\left(t_{rest}\right)=\tau_{00}+A_{thix}t_{rest} \tag{4.4}$$

with the rate of increase of the static yield stress of the material A_{thix} at rest. Substituting Eqs. (4.1), (4.2) and (4.4) in Eq. (4.3), the inequality which shows the maximum resting time is expressed as follows

$$t_{rest}\leq\frac{\sqrt{\frac{\left(\rho gd\right)^{2}}{12}+\left(\tau_{00}+\mu_{p}\frac{2V}{d}\right)^{2}}-\tau_{00}}{A_{thix}} \tag{4.5}$$

For the case study, using the estimated plastic viscosity and yield stress from the previous chapter, the maximum resting time can be calculated. The parameters are chosen as below. The initial static yield stress is determined based on the time past after the material has been mixed, here, 15 min selected.

Table 4-6 Chosen parameters for calculating the maximum resting time

Parameters			Resting time
Density	ρ	1850 kg/m^3	298.9 sec
Acceleration of gravity	g	9.8 m/sec^2	
Depth of layer	d	0.01 m	
Print speed	V	0.1 m/sec	
Plastic viscosity	μ_p	11.53 Pa-sec	
Initial static yield stress	τ_{00}	2004.22 Pa	
Structuration rate	A_{thix}	0.7796 Pa/sec	

4.3 Hardened Concrete Properties

Additionaly, the compressive strength of the hardened concrete is measured after curing 7 days, 14 days and 28 days. Test samples are 50×50×50 volume cubes and are tested by UTM. The average compressive strengths are 41.4 MPa, 52.39 MPa and 66.64 MPa, respectively.

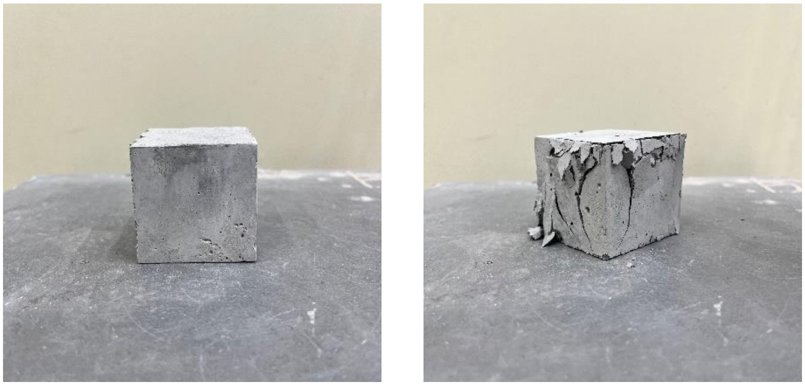

Figure 4-14 Hardened concrete cube for compressive strength test

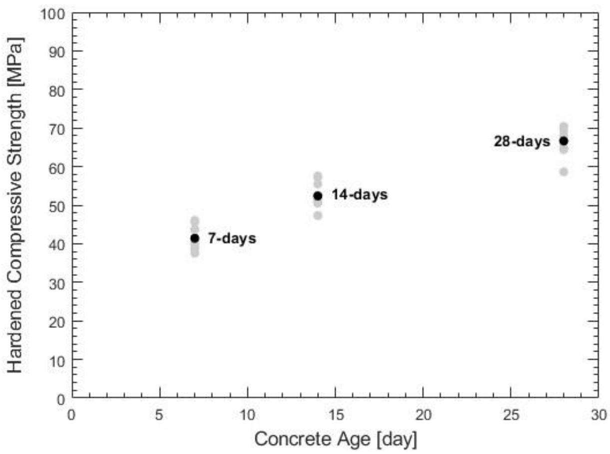

Figure 4-15 Compressive strength of hardened concrete in 7, 14 and 28 days

Chapter 5. Experimental Verification of 3D Printing

5.1 3D Printing Process

5.1.1 Experimental conditions

The 3D printing experiments were carried out using the material which has specific properties covered in the previous chapter at Korea Institue of Civil Engineering and Building Technology laboratory. The 3D concrete printer used was the grantry-type which has three axes movement and at least 40 liters of the concrete material is needed to operate the pump which is the screw type.

Figure 5-1 Gantry type 3D concrete printer, concrete blender and pump

The 10 meters hose was used and two types of nozzles, 13mm and 25mm, were used to make the parameter conditions, such as layer height and depth, α and structure growth velocity. The probability of buckling may be increased when the value of α decreases, which means using smaller nozzle is more appropriate for the test to measure the critical buckling length

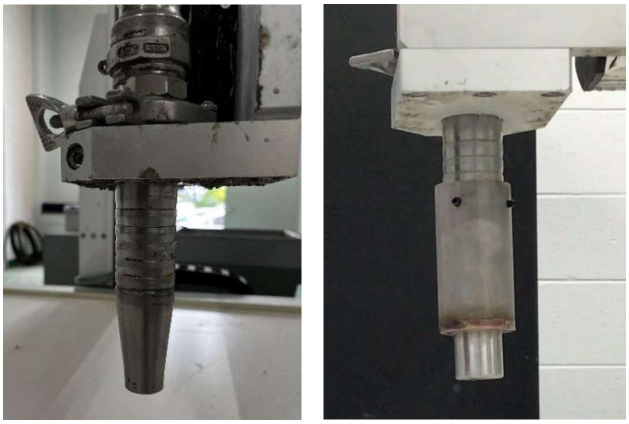

Figure 5-2 Two types of printing nozzles : 25mm and 13mm

5.1.2 Experimental specimens

By using 25 mm size nozzle, totally 19 samples were printed with the horizontal printing velocity, v_n = 0.07 m/sec. The actual printed layer height is larger than the nozzle size, since the material spreads on the lower layer during the discharge process. Average layer height when the 25 mm diameter nozzle is used is 30 mm and layer depth is 15mm. The layer height as h = 30 mm is used in the analysis, thus the α is 0.12 for the 250 mm radius structure.

Table 5-1 Geometric configurations and printing parameters of samples printed by 25 mm nozzle

Radius	α	T **[sec]**	$\dot{l}$ **[mm/s]**	**Number of specimens**
50 mm	0.6	4.52	3.32	5
62.5 mm	0.48	5.65	2.65	4
83.3 mm	0.36	7.53	1.99	4
125 mm	0.24	11.3	1.33	4
250 mm	0.12	22.6	0.66	2

Figure 5-3 250 mm radius 3D printed concrete structure with 25 mm nozzle

A total of 28 experiements were conducted by 13 mm size nozzle on 9 types of different geometric structures with v_n = 0.1 m/sec. Same as 25 mm nozzle, the actual printed layer height is 20 mm and nozzle depth is 10 mm which is larget than the size of nozzle.

Table 5-2 Geometric configurations and printing parameters of samples printed by 13 mm nozzle

Radius	α	T [sec]	$\dot{l}$ [mm/s]	Number of specimens
50 mm	0.4	3.12	3.21	3
62.5 mm	0.32	3.90	2.57	1
75 mm	0.27	4.68	2.14	1
83.3 mm	0.24	5.19	1.93	2
125 mm	0.16	7.79	1.28	3
150 mm	0.13	9.35	1.07	3
250 mm	0.08	15.58	0.64	4
300 mm	0.07	18.7	0.53	8
325 mm	0.06	20.26	0.49	3

Figure 5-4 300 mm radius 3D printed concrete structures with 13 mm nozzle

5.2 Comparison of Experimental and Analytical Results

5.2.1 3D printing with 25 mm diamaeter nozzle

A buckling behavior was detected from 50 mm radius sample at the early concrete age. However, the other specimens collapsed since the material at the bottom layer yielded. For some samples, yielding occurred more than two times. A part of the bottom layer yielded at first and other part yielded after more layers printed. Furthermore, after the cylindrical structure loses the stiffness due to the occurrence of yielding at the bottom, the shape of the structure was maintained and it did not collapse even if more layers were printed.

Table 5-3 Experimental results with h = 30 mm

Radius		**15 ~ 25 min**	**25 ~ 35 min**	**35 min ~**
50mm	Buckling	255mm (19)		
	Plastic	225mm (22)	255mm (25) 240mm (28)	270mm (41)
62.5mm	Plastic		225mm (29) 270mm (32)	240mm (35) 270mm (37)
83.33mm	Plastic	165mm, 210mm 225mm, 240mm (17) 195mm, 225mm (20) 255mm, 285mm (21)		240mm, 285mm (41)
125mm	Plastic	180mm, 195mm 210mm, 240mm (22) 240mm, 285mm 330mm (24)	180mm, 210mm 225mm (25)	240mm, 285mm 300mm, 345mm 375mm (45)
250mm	Plastic		255mm, 285mm (29)	240mm, 285mm 390mm (37)

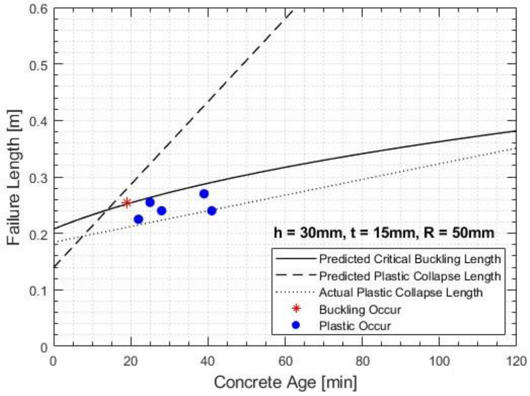

Figure 5-5 Results from 50 mm radius cylindrical structure with h = 30 mm

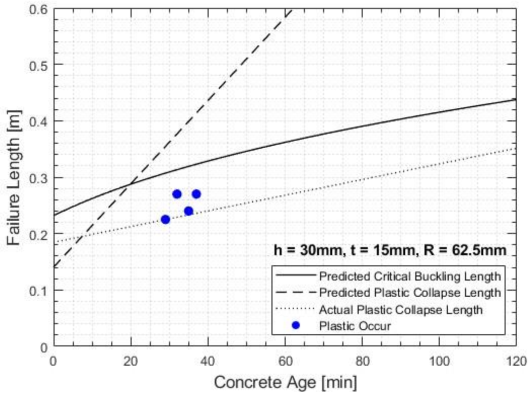

Figure 5-6 Results from 62.5 mm radius structure with h = 30 mm

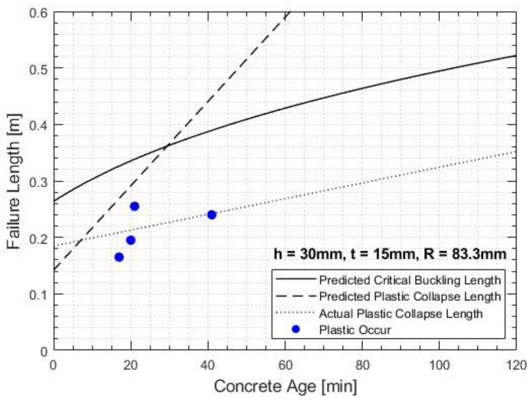

Figure 5-7 Results from 83.3 mm radius structure with h = 30 mm

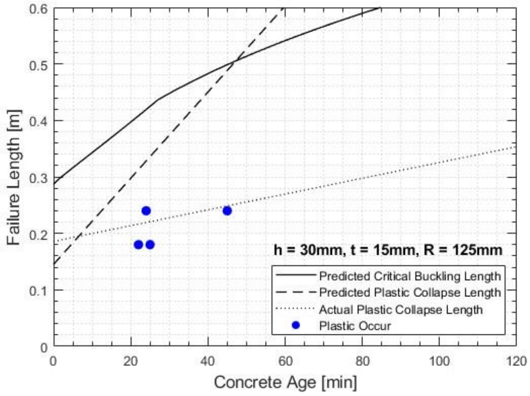

Figure 5-8 Results from 125 mm radius structure with h = 30 mm

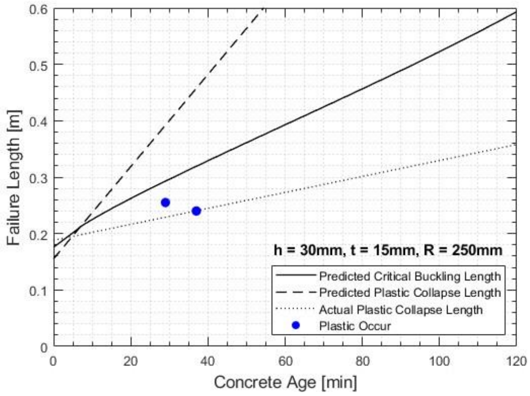

Figure 5-9 Results from 250 mm radius structure with h = 30 mm

The buckling length from the 50 mm radius sample is greater than the predicted buckling length of shell model. The other points that plastic collapse occurred are located below the prediction curve. However, 70 percents of them are above the actual plastic collapse length which is estimated by the validation experiment data and below the predicted critical buckling length

5.2.2 3D printing with 13 mm diameter nozzle

More occurrence of the buckling is expected by using smaller nozzle since the α value gets smaller than the bigger nozzle in the case of the structure having same radius.

Table 5-4 Experimental results with h = 20 mm

Radius		**15 ~ 40min**	**40 ~70 min**	**70 min ~**
50mm	Plastic	199mm (32)	290mm (63)	292mm (93)
62.5mm	Plastic			283mm (90)
75mm	Plastic	193mm (25)		
83.33mm	Plastic	193mm, 229mm (26)		283mm (70)
125mm	Plastic	229mm, 256mm (31)	211mm, 265mm (42)	265mm (84)
150mm	Buckling		220mm (67)	
	Plastic	220mm (29)		265mm (73)
250mm	Buckling		211mm (51)	
	Plastic		274mm (60)	256mm (73) 326mm (108)
300mm	Buckling	202mm (19) 202mm (26)	309mm (45) 301mm (50)	352mm (79)
	Plastic	220mm (36)		256mm (73) 335mm (85)
325mm	Buckling	165mm (36)		292mm (86)
	Plastic		256mm (46)	

The buckling occurred 9 times especially for the 300 mm radius structures.

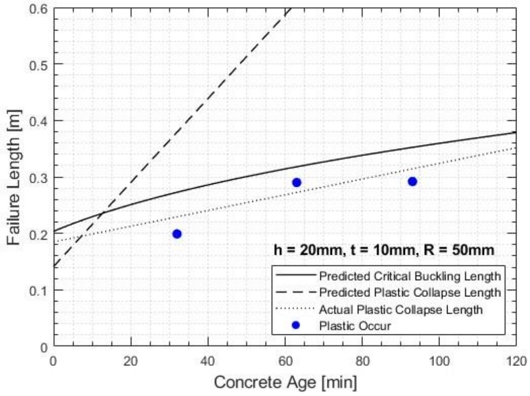

Figure 5-10 Results from 50 mm radius cylindrical structure with h = 20 mm

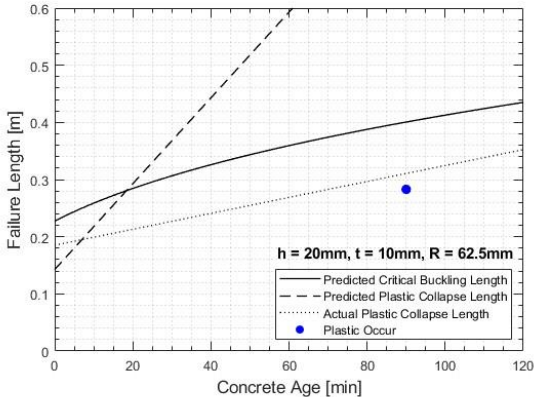

Figure 5-11 Results from 62.5 mm radius structure with h = 20 mm

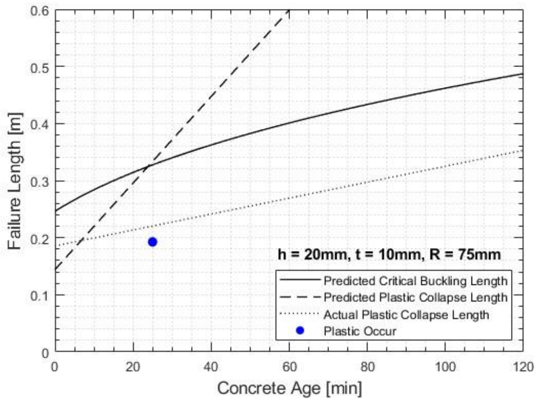

Figure 5-12 Results from 75 mm radius structure with h = 20 mm

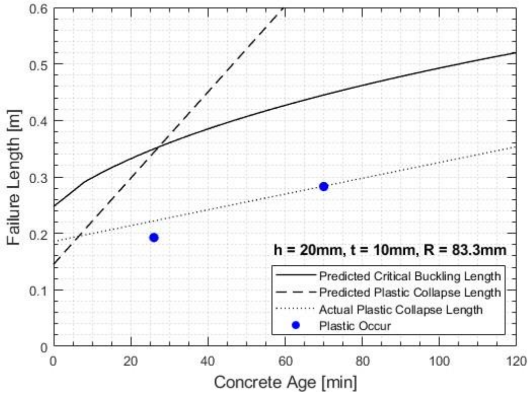

Figure 5-13 Results from 83.3 mm radius structure with h = 20 mm

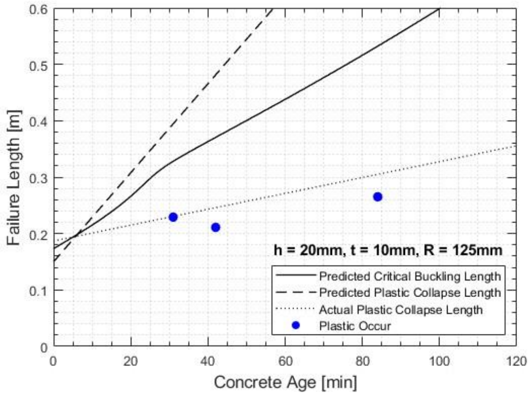

Figure 5-14 Results from 125 mm radius structure with h = 20 mm

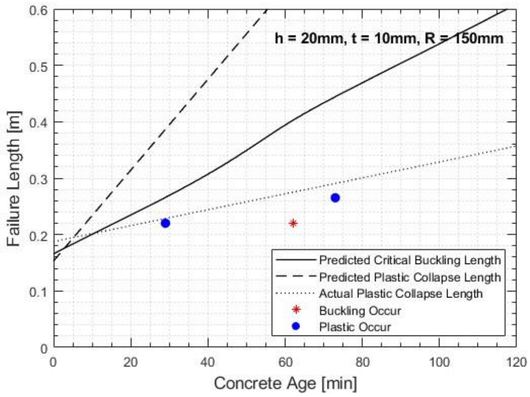

Figure 5-15 Results from 150 mm radius structure with h = 20 mm

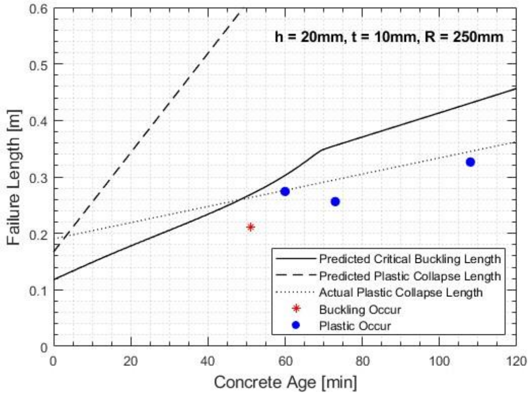

Figure 5-16 Results from 250 mm radius structure with h = 20 mm

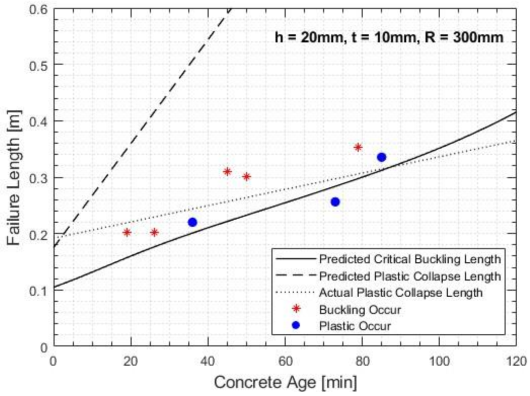

Figure 5-17 Results from 300 mm radius structure with h = 20 mm

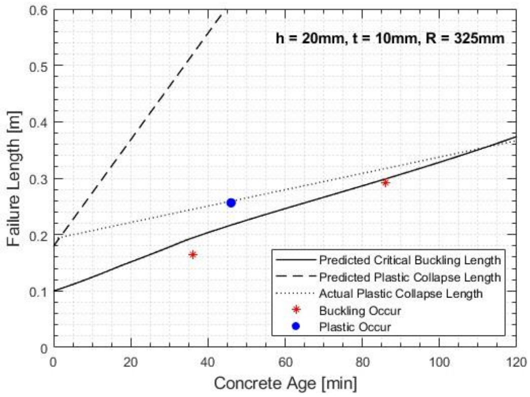

Figure 5-18 Results from 325 mm radius structure with h = 20 mm

5.3 Summary

5.3.1 Error between experimental data and prediction for buckling length and buckling mode

The differences between the critical buckling length from the validation experiment and numerical analysis are arranged as table below.

Table 5-5 Result comparison for the buckling length between experimental data and prediction

h - R - (min)	Experiment	Prediction	Error
30 - 50 - (19)	255 mm	252 mm	+1.2 %
20 - 150 - (67)	220 mm	422 mm	-47.8 %
20 - 250 - (51)	211 mm	268 mm	-21.3 %
20 - 300 - (19)	202 mm	158 mm	+27.7 %
20 - 300 - (26)	202 mm	178 mm	+13.4 %
20 - 300 - (45)	309 mm	222 mm	+39.3 %
20 - 300 - (50)	301 mm	233 mm	+29 %
20 - 300 - (79)	352 mm	298 mm	+18.3 %
20 - 325 - (36)	165 mm	194 mm	-15.1 %
20 - 325 - (86)	292 mm	299 mm	-2.4 %

The errors between actual data and predition are ranged from -47.8 % to +39.3 %. Half of the bucklings occurred from the 300 mm radius cylindrical structure with h = 20 mm and the lengths of the structures when they collapse were always higher than predicted. Otherwise, most of them collapsed below the estimated length.

Furthermore, most of samples show same buckling mode as predicted when they collpased. Samples which collapsed with lower or higher buckling mode than estimated had large error for comparison of buckling length.

Table 5-6 Result comparison for the buckling mode between experimental data and prediction

h **-** ***R*** **- (min)**	**Experiment**	**Prediction**
30 - 50 - (19)	1	1
20 - 150 - (67)	2	2
20 - 250 - (51)	<u>2</u>	3
20 - 300 - (19)	3	3
20 - 300 - (26)	3	3
20 - 300 - (45)	<u>2</u>	3
20 - 300 - (50)	3	3
20 - 300 - (79)	3	3
20 - 325 - (36)	<u>4</u>	3
20 - 325 - (86)	3	3

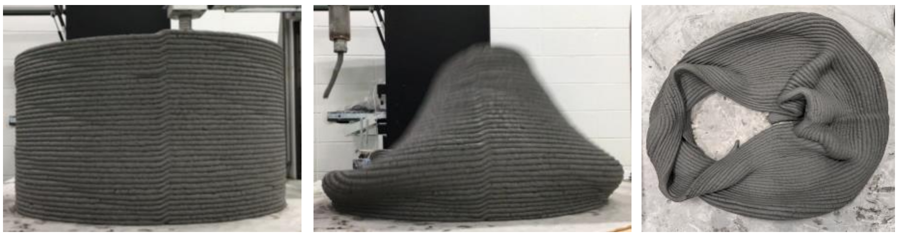

Figure 5-19 Sequence of experimental verification

5.3.2 Actual compressive strength from experiments

The compressive strength of the material which is used for the validation experiement is already measured from Chapter 4.2.2. However, when the stresses obtained from the samples, which were collapsed by yielding at the bottom layer, are plotted, all of experimental data are located under the measured compressive strength and has lower slope. This figure indicates that the compressive strength changes after pupmped or while the material is passing through the pipe.

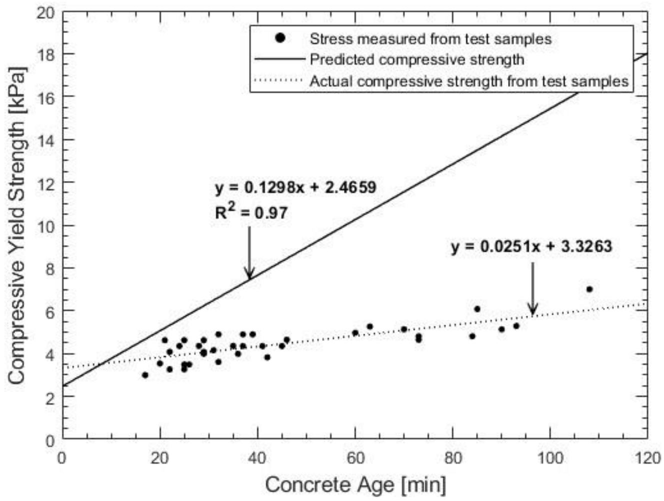

Figure 5-20 Different compressive strength curve during printing

5.4 Discussion

From the experimental verification process, some data are located below the predicted curves and failed by plastic collapse unexpectively. The actual material properties which are discharged from the printing nozzle are different from the measured material properties as Figure 5-20, since the material during the pumping or on the way through the hose is re-mixed. Thus, the properties are changed which can not be measured accurately, since the various printing conditions influence to them in combination. Furthermore, the actual strengths and stiffness are expected to be lower than measured from the static condition, since the curing effect of material does not occur as well as expected during printing process. As a result, samples which are estimated to have high stiffness and strength collapsed at a different length and by a different failure mode from the prediction. The other reason why some samples collapsed below the predicted failure length and collapsed by different failure mode is the effect of the eccentricity. In the numerical anaylsis process, the model assumes the length of structure increases consistenly. However, in actual printing process, the layer having the specific thickness is printed on the lower layer and this condition occurs asymmetry loading along the circumference. In addition, due to this limitation, the deformation does not occur simultaneously in the circumferential direction, and it leads to the geometric imperfection. Thus, a stiffness of cylindrical structure decreases and a stress on a part of layer being printed increases than prediction.

Chapter 6. Conclusion

The mechanical performance of cylindrical structures during the 3D printing process can be analysied by using the model suggested in this paper. The model distinguishes between the failure mode by elastic global buckling, elastic local buckling and plastic collapse. The cylindrical column model is used for analyzing elastic global buckling and the shell model for elastic local buckling. These models consider the curing effect of the material as linear function and analyze in the dimensionless coordinate system. The column model predicts the failure length always higher than shell model while the difference can be almost negligible at specific condition. The shell model provides the critical buckling length and corresponding buckling mode. Generally, as the raidus of structure increases, it buckles at the low length while other parameters are constant. In addition, by considering the effect of geometric imperfection to the shell model, the decrease in stiffness of structure and the change in buckling response are identified. Plastic collapse failure relates to the stress at the bottom layer and the yield strength of the material, affected from the material properties. The model results are summarized in the design graphs which have different conditions and these graphs provides the practical tool for predicting the performance of arbitrary cylindrical structure under the broad range of possible conditions. The column model, reflecting the global buckling, provides the upper bound to the elasic buckling length while the shell model, corresponding to the local buckling, gives the lower bound according to the buckling mode. The failure length for plastic collapse may narrow or widen the boundary boundary, determining the governing failure mode of the cylindrical structure under specific conditions. This can be demonstrated by the case study which shows the governing failure mode according to the conditions. The properties of material, such as the intial modulus of elasticity, compressive strength and yield stress, are measured and each property shows linear increasing. Assuming the curing function for material properties as the linear evolution in the anaylsis process is verified. The accuracy of the proposed model can be shown from experimental validation and the model underestimates the buckling length in most cases. The models can be utilized as a design or validation tool for 3D printed cylindrical structures.

References

[1] F42 Committee, n.d. Terminology for Additive Manufacturing Technologies,. ASTM International.

[2] Lee, I.H., Kim, H.-C., Ahn, D.-G., 2020. Korean Terminologies for Additive Manufacturing according to the ISO/ASTM 52900 Standard. KSPE 37, 929–936.

[3] Tay, Y.W.D., Panda, B., Paul, S.C., Noor Mohamed, N.A., Tan, M.J., Leong, K.F., 2017. 3D printing trends in building and construction industry: a review. Virtual and Physical Prototyping 12, 261–276.

[4] Hou, S., Duan, Z., Xiao, J., Ye, J., 2021. A review of 3D printed concrete: Performance requirements, testing measurements and mix design. Construction and Building Materials 273, 121745.

[5] Suiker, A.S.J., 2018. Mechanical performance of wall structures in 3D printing processes: Theory, design tools and experiments. International Journal of Mechanical Sciences 137, 145–170.

[6] Shell Buckling [WWW Document], n.d. URL https://shellbuckling.com/index.php (accessed 12.22.21).

[7] Lim, C.W., Ma, Y.F., 2003. Computational p -element method on the effects of thickness and length on self-weight buckling of thin cylindrical shells via various shell theories. Computational Mechanics 31, 400–408.

[8] Timoshenko, S.P., Gree, 1963. Theory of elastic stability.

[9] Wolfs, R.J.M., Bos, F.P., Salet, T.A.M., 2018. Early age mechanical behaviour of 3D printed concrete: Numerical modelling and experimental testing. Cement and Concrete Research 106, 103–116.

[10] Roussel, N., Cussigh, F., 2008. Distinct-layer casting of SCC: The mechanical consequences of thixotropy. Cement and Concrete Research 38, 624–632.

[11] Roussel, N., 2006. A thixotropy model for fresh fluid concretes: Theory, validation and applications. Cement and Concrete Research 36, 1797–1806.

[12] Timoshenko, S.P., Gree, 1951. Theory of elastic.

[13] Timoshenko, S.P., Gree, 1959. Theory of plates and shells.

초 록

콘크리트 원형 중공 단면 구조물의 3D 프린팅 출력 중 구조적 안전성

정 승 수

서울대학교 건축학과 대학원

3D 프린팅 시공 중 자중에 의한 붕괴를 방지하는 것은 3D 프린팅 구조물의 주요 고려 사항이다. 출력 중에는 낮은 강성과 강도를 가지는 굳지 않은 상태의 콘크리트 재료를 사용하기 때문에, 설계 또는 시공 과정에서 한 번에 출력 가능한 최대 높이를 계산해야 한다. 본 논문에서는 원형 중공 단면 구조물의 3D 프린팅 중 기계적 성능을 해석하고 출력 파라미터를 최적화하는데 사용할 수 있는 역학 모델을 제안한다. 탄성 좌굴과 탄성 국부 좌굴, 그리고 소성 붕괴, 3 종류의 붕괴 메커니즘을 고려한다. 각각의 붕괴 종류에 대해서 기둥 모델, 쉘 모델 그리고 항복 조건을 사용한다. 모델은 재료의 특성, 기하학적 특징 그리고 프린팅 변수와 같은 다양한 변수들을 포함한다. 콘크리트 재료의 특징인 경화 효과는 구조물 모델링 시 높이 방향으로 일정하지 않은 강성과 강도에 의해 고려된다. 무차원 좌굴 길이에 대해 먼저 해석을 진행한 후,

두 좌굴 모델 사이의 결과값을 디자인 그래프에서 비교한다. 한편, 무차원 소성 붕괴 길이는 다른 좌표축에 대해서 예측되며, 좌굴 그래프와 같이 나타낼 수 없다. 모든 파라미터가 결정된 특정 구조물에 대한 사례 연구는 수치 해석 결과를 분석하는 과정을 보여준다. 또한, 특정 상황에서 지배하는 좌굴 메커니즘과 대응하는 좌굴 모드를 알 수 있다. 기존에 선형 함수 형태로 가정된 경화 특성은 재료 특성을 측정하는 실험을 통해 검증할 수 있다. 다양한 반지름을 가지는 원형 구조물에 대해 출력 실험을 진행하여 얻은 데이터와 모델로부터 예측된 붕괴 높이를 비교하여 모델의 정확도를 검증한다. 본 모델은 임의의 원형 구조물의 역학적 성능에 대한 각 출력 변수들의 영향을 알아내고, 붕괴 높이와 붕괴 메커니즘을 예측하는 모델로 사용될 수 있다.

주요어 : 3D 프린팅, 원형 중공 단면 구조물, 이종 재료, 좌굴, 소성 붕괴, 수치 해석, 디자인 그래프

학 번 : 2021-24853